Numerical Simulations of Seismoacoustic Nuisance Patterns from an Induced *M* 1.8 Earthquake in the Helsinki, Southern Finland, Metropolitan Area

Lukas Krenz[1], Sebastian Wolf[1], Gregor Hillers[2], Alice-Agnes Gabriel[*3,4], and Michael Bader[1]

ABSTRACT

Seismic waves can couple with the atmosphere and generate sound waves. The influence of faulting mechanisms on earthquake sound patterns provides opportunities for earthquake source characterization. Sound radiated from earthquakes can be perceived as disturbing, even at low ground-shaking levels, which can negatively impact the social acceptance of geoengineering applications. Motivated by consistent reports of felt and heard disturbances associated with the weeks-long stimulation of a 6-km-deep geothermal system in 2018 below the Otaniemi district of Espoo, Helsinki, we conduct fully coupled 3D numerical simulations of wave propagation in the solid Earth and the atmosphere. We assess the sensitivity of the ground shaking and audible noise distributions to the source geometry of the induced earthquakes based on the properties of the largest local magnitude M_L 1.8 event. Utilizing recent computational advances and the open-source software SeisSol, we model seismoacoustic frequencies up to 25 Hz, thereby reaching the lower limit of the human audible sound frequency range. We present synthetic distributions of shaking and audible sounds at the 50–100 m scale across a 12 km × 12 km area and discuss implications for better understanding seismic nuisances in metropolitan regions. In five 3D coupled elastic–acoustic scenario simulations that include data on topography and subsurface structure, we analyze the ground velocity and pressure levels of earthquake-generated seismic and acoustic waves. We show that *S* waves generate the strongest sound disturbance with sound pressure levels ≤ 0.04 Pa. We use statistical analysis to compare our noise distributions with commonly used empirical relationships. We find that our 3D synthetic amplitudes are generally smaller than the empirical predictions and that the interaction of the source mechanism-specific radiation pattern and topography can lead to significant nonlinear effects. Our study highlights the complexity and information content of spatially variable audible effects associated with small induced earthquakes on local scales.

KEY POINTS

- We model coupled seismic and sound wave propagation at a 6-km-deep geothermal system in Helsinki.
- We assess the sensitivity of ground shaking and audible noise distributions to the earthquake source geometry.
- Our study has important implications toward a better understanding of seismic nuisances in metropolitan regions.

INTRODUCTION

Induced seismicity is essential to increase the reservoir flow rate in an enhanced geothermal system (EGS). Hence, the mitigation of damaging earthquake ground motions is important for this and other geoengineering applications. This is why increasing attention has been paid to the assessment of acceptable ground shaking limits associated with anthropogenic

1. TUM School of Computation, Information and Technology, Department of Computer Science, Technical University of Munich, Munich, Germany, https://orcid.org/0000-0001-6378-0778 (LK); https://orcid.org/0009-0000-4334-1938 (MB); 2. Institute of Seismology, University of Helsinki, Helsinki, Finland, https://orcid.org/0000-0003-2341-1892 (GH); 3. Scripps Institution of Oceanography, UC San Diego, La Jolla, California, U.S.A., https://orcid.org/0000-0003-0112-8412 (A-AG); 4. Department of Earth and Environmental Sciences, Ludwig-Maximilians-Universität München, Munich, Germany

*Corresponding author: algabriel@ucsd.edu

Cite this article as Krenz, L., S. Wolf, G. Hillers, A.-A. Gabriel, and M. Bader (2023). Numerical Simulations of Seismoacoustic Nuisance Patterns from an Induced *M* 1.8 Earthquake in the Helsinki, Southern Finland, Metropolitan Area, *Bull. Seismol. Soc. Am.* **113**, 1596–1615, doi: 10.1785/0120220225

seismicity (e.g., Brooks *et al.*, 2018; Keil *et al.*, 2022). In contrast, the excitation of potentially disturbing audible effects appears to be of minor (Megies and Wassermann, 2014) or no concern (Majer *et al.*, 2012). However, audible earthquake signals (rumbling, roaring, sonic booms, clattering, or muffled sounds) have been reported in epicentral areas of large and small events (Davison, 1938; Ebel *et al.*, 1982; Sylvander *et al.*, 2007; Hill, 2011). Earthquake sound patterns have been linked to faulting mechanisms, which implies the possibility of noninstrumental earthquake source characterization from sufficiently dense and complete macroseismic surveys (e.g., Tosi *et al.*, 2000; Mäntyniemi, 2004).

The 2018 and 2020 deep geothermal stimulation experiments in the Helsinki metropolitan area have led in total to more than 300 macroseismic reports of felt and heard earthquake effects (Ader *et al.*, 2019; Hillers *et al.*, 2020; Lamb *et al.*, 2021; Rintamäki *et al.*, 2021). This demonstrates that persistent earthquake noise has the potential to negatively affect the public attitude toward stimulation activities (Stauffacher *et al.*, 2015). Research into local audible sound excitation mechanisms of small earthquakes can therefore support a smoother implementation of geothermal systems that are ideally developed near a large consumer base, which may express concerns about nuisances associated with vibrations and noise related to the stimulation.

Monitoring procedures and intervention protocols, including traffic light systems (TLSs), typically focus on the limitation of earthquake magnitude or other decision variables to prevent shaking levels that are hazardous to infrastructure or pose a nuisance to affected communities (Bommer *et al.*, 2006). Baisch *et al.* (2019) recalls implicit assumptions for TLS operations, most notably the belief that real-time responses to stimulated seismicity can prevent an increase in earthquake size after the action. Examples of TLS failures, such as the post-injection earthquake of the 2006 Basel, Switzerland, stimulation (Häring *et al.*, 2008), highlight the dependence of a successful TLS implementation on the employed forecast model. Forecast models cannot only be based on simple frequency–magnitude relationships but can also be composed of complex systems that include multiphysics feedback mechanisms between the injected fluids and monitored seismicity (Gaucher *et al.*, 2015). The latter can be a key module in an operational strategy that constantly adapts to evolving situations (Grigoli *et al.*, 2017; Mignan *et al.*, 2017). The definition of TLS threshold values, such as tolerable earthquake magnitude, can appear ad hoc (Baisch *et al.*, 2019). Structurally safe shaking levels may still reach an intensity that is unacceptable to a critical part of the public (Rutqvist *et al.*, 2014). This is addressed by approaches that highlight the need for spatially varying limit definitions instead of single-valued thresholds for a larger area, and consider probabilistic models of perceptible ground shaking for TLS threshold determination (Schultz, Beroza, and Ellsworth, 2021; Schultz, Quitoriano, *et al.*, 2021). State-of-the-art mitigation strategies do not consider acoustic emissions or noise generation (Verdon and Bommer, 2021). This reflects the preconception that "seismicity usually does not radiate sufficient noise to be audible" (Majer *et al.*, 2012), although this topic is recognized in geothermal energy social acceptance studies ("many residents … are afraid of noise"; Stauffacher *et al.*, 2015).

Public perception of induced seismic effects, including sound, can be potentially critical to geothermal project management. This requires a broad knowledge base of the physical mechanisms for sound generation and quantification of these effects to inform tailored mitigation strategies and region-specific solutions. Key questions related to sound generation associated with subsurface seismic sources include whether sound excitation is confined to the epicentral area, whether sound waves are locally generated through seismoacoustic coupling, or whether secondary sources associated with topography play a dominant role (Arrowsmith *et al.*, 2010; Lamb *et al.*, 2021), and how meteorological conditions affect propagation. These questions are relevant to seismoacoustic waves at all frequencies, regardless of whether sound waves are audible or not.

Epicentral, local, or diffracted earthquake infrasound, or inaudible sound, with a frequency content below 20 Hz can be excited by the coupling of *P* waves, *S* waves, and surface waves (Mutschlecner and Whitaker, 2005; Evers *et al.*, 2014; Hernandez *et al.*, 2018; Shani-Kadmiel *et al.*, 2021). Infrasound observations are supported by a mature network of global permanent infrasound sensors (Hedlin *et al.*, 2012; Hupe *et al.*, 2022), and temporary network densification (Vernon *et al.*, 2012) allows locally higher resolution of transient local phenomena (Edwards *et al.*, 2014). Modeling of seismoacoustic coupling may include atmospheric propagation effects. Studies of infrasound propagation from sources to receivers across regional and global distances generally account for the 3D atmospheric structure between the ground and heights up to an altitude of 120 km in the thermosphere. Ray tracers (Arrowsmith *et al.*, 2010), propagation models based on the parabolic equations of infrasound (Waxler *et al.*, 2022), or other approaches (Waxler and Assink, 2019) include the effects of wind and temperature that also govern dissipation.

Audible earthquake noise patterns excited by small to moderate earthquakes (Sylvander and Mogos, 2005; Thouvenot *et al.*, 2009; Mäntyniemi, 2022) on local scales, which are relevant here, are often approximated using relationships between vertical ground motion and induced sound pressure that disregard atmospheric propagation effects (Hill *et al.*, 1976; Tosi *et al.*, 2000; Lamb *et al.*, 2021). Compared to infrasound data, audible noise observations are sparse; however, increasingly dense high-frequency sound observations increase the demand for excitation and propagation models with comparable resolution.

Macroseismic report patterns across Helsinki (Hillers *et al.*, 2020) show strong spatial variations at the district or

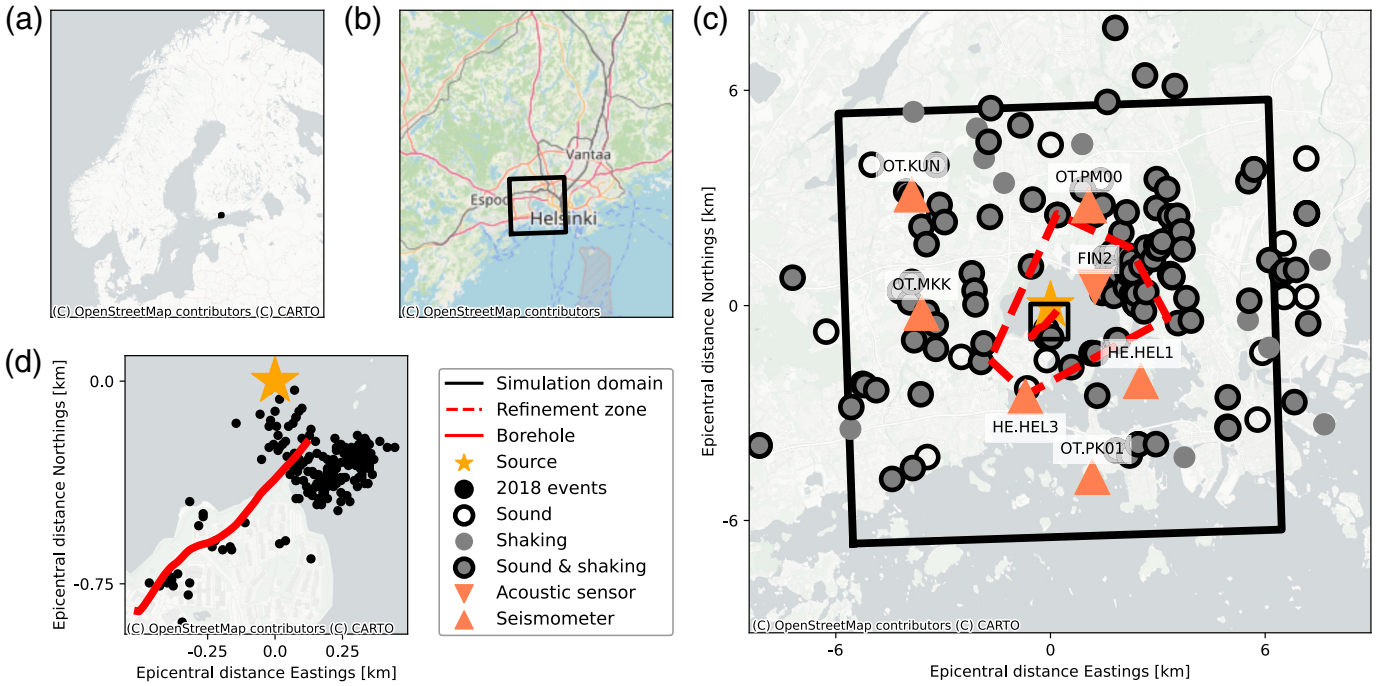

Figure 1. (a) Location of the study area in northern Europe; the black symbol marks the location of the black squares in panels (b) and (c). (b) Location of the study area in the Helsinki metropolitan area. The black square indicates the computational domain, as shown in panel (c). (c) Circles show the locations of all 220 macroseismic reports submitted during the 2018 stimulation period. Their locations are accurate to the street addresses. Circles with black outlines indicate reported sound observations. The gray circles (no outline) indicate the reported shaking sensations. The gray circles with black outlines represent observations of both sound and shaking. The large black square indicates the 12 km × 12 km simulation domain. The small black square in the center shows the epicentral area enlarged in panel (d). The red dashed polygon encloses the source region and neighborhoods to the northeast, from where many macroseismic reports were collected. In this region, we compute the seismoacoustic wavefields with the highest accuracy. The inverted triangle indicates the location of the FIN2 microphone array (Lamb *et al.*, 2021), and the other triangles indicate the selection of seismic stations that we use for data comparison. The star indicates the location of the largest induced M_L 1.8 event 13 in Hillers *et al.* (2020). All figures use this location as the origin. (d) The 2018 borehole trajectory is indicated in red, as in panel (c). The borehole is vertical down to a depth of 5000 m and then inclines in the northeast direction. The black symbols show 203 manually revised event locations (Hillers *et al.*, 2020), which are a small subset of the several thousands of induced earthquakes. All maps use the Webmercator coordinate system, which is different from the map projection used for the simulations. The color version of this figure is available only in the electronic edition.

neighborhood scale (Fig. 1). This highlights the need to accurately model small-scale complexities of seismoacoustic energy coupling and propagation at frequencies that include at least the lower limit of the human audible frequency range around 20 Hz. The Helsinki stimulation was conducted in the southern Finland Fennoscandian Shield environment. The absence of sedimentary layers means that the 6 km deep stimulated bedrock units crop out and high-frequency seismic energy reaches the surface. This geological situation leads to recurrently observed felt and heard experiences reported by an urban population unfamiliar with earthquake phenomena. The models presented here can quantitatively support research into geological, infrastructural, socioeconomic, or other factors that govern public response pattern. However, the inherent small length scales and multiphysics characteristics pose serious challenges to numerical approaches.

Advances in high-performance computing facilitate the investigation of the generation and propagation of a variety of seismoacoustic signals, including the generation of ultra-low-frequency acoustic *T* waves in 2D and 3D simulations (e.g., Averbuch *et al.*, 2020; Che *et al.*, 2022). However, 3D coupled seismoacoustic simulations remain computationally challenging. For example, Lecoulant *et al.* (2019) modeled oceanic *T* waves using the spectral element code SPECFEM3D with an idealized bathymetry across a 200 km × 50 km domain and resolving seismic waves up to 2.5 Hz, resulting in a 560,000 finite-element mesh. The simulation ran for 8 hr on 336 parallel processors to compute 200 s waveforms. Brissaud *et al.* (2017) coupled SPECFEM2D to a compressible Navier–Stokes solver to simulate seismogravito acoustic waves. A 3D fully coupled elastic–acoustic simulation of the 2018 Palu, Sulawesi, earthquake and tsunami using the Discontinuous Galerkin code SeisSol and a mesh with 518 million elements (261 billion degrees of freedom) used 3072 nodes (147,456 compute cores) of the supercomputer SuperMUC-NG and took 5.5 hr to compute 30 s of the event (Krenz *et al.*, 2021). Seismically induced acoustic signals in air travel more slowly, thus requiring more refined meshes than ocean acoustic models to resolve the relevant frequencies.

Modeling high-frequency seismoacoustic wavefields in 3D therefore requires expensive numerical simulations using substantial computational resources on supercomputers because the number of required degrees of freedom typically scales with the minimum velocity and the highest resolved frequency (e.g., Käser *et al.*, 2008). We use the open-source seismic wave propagation software SeisSol, which achieves a sustained high-computational performance in the petascale range (Dumbser and Käser, 2006; Uphoff *et al.*, 2017; Krenz *et al.*, 2021; Ulrich *et al.*, 2022). SeisSol has been extended to simulate coupled elastic–acoustic and tsunami gravity wave propagation (Krenz *et al.*, 2021; Abrahams *et al.*, 2023). These advances allow us to numerically study the sensitivity of ground shaking and sound patterns to varying source properties.

We compute high-resolution seismic and acoustic wave propagation scenarios across a 12 km × 12 km area with a subelement refinement of up to 2.3 m. Our model is based on the largest M_L 1.8 reference earthquake, event 13 in Hillers *et al.* (2020), induced during the Helsinki geothermal stimulation. We design and validate our simulations using the observed earthquake properties, a local velocity model, seismic ground-motion measurements, acoustic recordings, and macroseismic reports (Fig. 1).

In The Stimulation Experiment, Data, and Macroseismic Reports section, we summarize the Helsinki stimulation experiment and associated macroseismic reports that motivated our study. In the Numerical Experiments section, we explain our multiphysics 3D model for fully coupled elastic–acoustic wave propagation scenarios in the Helsinki metropolitan area, which incorporates high-resolution topography data. In the Results section, we verify the numerical solution with seismic data and acoustic measurements. We evaluate the effect of the source mechanism on the computed shaking and sound distributions, which can be important data for modeling nuisance maps, as well as the consistency of the spatial variability of synthetic shaking and sound excitation with macroseismic observations. Our analysis separates effects associated with *P*-wave and *S*-wave energy to assess the relative contribution of different body-wave phases to sound disturbances. This allows us to evaluate the compatibility of common assumptions and simplifications when approximating noise disturbance levels from seismic ground velocities. The implications and limitations of our results are discussed in the Discussion section.

THE STIMULATION EXPERIMENT, DATA, AND MACROSEISMIC REPORTS

In this section, we summarize the relevant data and observations associated with the Helsinki stimulation experiment that form the background for our study. We study the seismic and acoustic wave excitations in response to two stimulations intended to establish a geothermal doublet system for district heating around 6 km below the Aalto University campus in Otaniemi, a district in the city of Espoo next to Helsinki (Fig. 1). The majority of the induced seismicity is located below the shallow, ∼10 m deep, and ∼3 km wide Laajalahti Bay. During the first larger stimulation in June and July 2018, approximately 18,000 m^3 of freshwater was pumped into the deep crystalline rock formation, which induced thousands of small earthquakes (Kwiatek *et al.*, 2019). During the second smaller counter stimulation in May 2020, a total volume of 2900 m^3 of water was used, and the seismic response was weaker (Kwiatek *et al.*, 2022). In 2018, seismicity was organized into three clusters between 5 and 6.5 km depth (Kwiatek *et al.*, 2019). A small cluster formed in response to the 2020 stimulation alongside the largest and deepest 2018 cluster (Kwiatek *et al.*, 2022). The 600 × 1200 m^2 lateral patch size of the seismicity around the two northeast-striking deep open-hole sections indicates that the source region is relatively compact compared to the area affected by the induced wavefields. The local geology is characterized by Precambrian bedrock units. Outcropping bedrock in backyards and open spaces is a common sight in the Helsinki area as it occupies approximately 25% of the surface area. The other parts are covered by meter thick deposits of gravel, sand, clay, or peat. Vegetated areas often thrive on a centimeter thick topsoil layer covering the rocks. At the topmost tens of meters, weathering processes have led to an approximately 50% reduction compared with the high seismic basement rock velocities (Hillers *et al.*, 2020).

The seismic response to the stimulations was monitored using a 2 km deep borehole string, 12 shallow borehole stations (Kwiatek *et al.*, 2019), and a surface station network consisting of more than 100 sensors organized as single stations and mini arrays (Hillers *et al.*, 2020; Rintamäki *et al.*, 2021). Most stations were installed within a distance of 20 km from the wellhead. High sampling rates are essential for resolving the high-frequency energy of induced seismic wavefields that reach the surface. Between 7 and 18 July 2018, the operating St1 Deep Heat Oy installed two temporary microphone arrays, FIN1 and FIN2, at sites 2.2 km to the northeast and 2.5 km to the west from the wellhead (Lamb *et al.*, 2021). The seismic data support a number of studies focusing to date on real-time monitoring (Ader *et al.*, 2019), reservoir and seismicity characterization (Kwiatek *et al.*, 2019, 2022; Bentz *et al.*, 2020; Leonhardt *et al.*, 2021; Holmgren *et al.*, 2023), and wave-propagation effects (Li *et al.*, 2021; Taylor *et al.*, 2021). Eulenfeld *et al.* (2023) estimated high anelastic Q values around 3×10^5 in the 10–40 Hz range and similarly high scattering Q values around 1×10^5. This exceptionally low attenuation explains the observed high transparency of seismoacoustic waves at human-audible frequencies (Lamb *et al.*, 2021).

A three-tier traffic-light system was defined. For this, the probabilities to exceed peak ground velocity (PGV) and peak ground acceleration thresholds were linked to local earthquake magnitudes using ground-motion prediction equations (Ader

et al., 2019). The green, amber, and red PGV thresholds are 0.3 mm s^{-1}, 1 mm s^{-1}, and 7.5 mm s^{-1}, respectively. The thresholds are set to minimize cosmetic building damage in accordance with building codes. In addition, macroseismic effects on human perception are considered (Westaway and Younger, 2014; Bommer *et al.*, 2017). The amber and red maximum local magnitude (Uski and Tuppurainen, 1996) limits were M_L 1.2 and 2.1, respectively. An adaptive injection protocol, partially based on earthquake physics (Galis *et al.*, 2017), helped control the largest estimated magnitudes of M_L 1.8 and 1.2 during the 2018 and 2020 stimulations (Ader *et al.*, 2019; Kwiatek *et al.*, 2019, 2022).

Although no event exceeded the threshold magnitude, the public reported 220 and 111 individual observations of ground shaking and audible disturbances to the macroseismic questionnaire of the Institute of Seismology, University of Helsinki, in 2018 and 2020, respectively (Hillers *et al.*, 2020; Rintamäki *et al.*, 2021). In 2018, the number of responses scaled approximately exponentially with magnitude (Ader *et al.*, 2019), that is, the distribution did not saturate toward the typically observed sigmoid function (Schultz, Quitoriano, *et al.*, 2021). Scattered reports started to trickle in for magnitudes around M_L 1.0, and a maximum of 83 reports was received after the largest M_L 1.8 event. The response patterns are modulated by the activity level, and during the 2020 stimulation, local COVID-19 mobility restrictions likely played a role in the comparatively increased reporting activity (Rintamäki *et al.*, 2021). Locations are available by street address, which shows that a reporting center is located around the Munkkivuori neighborhood about 3 km northeast of the injection site. Most other reports arrived from a north–south-oriented 5 km × 10 km large area bordering the drill site to the west.

Humans can generally perceive sounds in the range of 20 Hz–20 kHz (Fastl and Zwicker, 2006). Sound at 20–200 Hz is called low-frequency sound, and infrasound refers to the generally inaudible range below 20 Hz (e.g., Møller and Pedersen, 2004). Infrasound is excited by natural phenomena including wind, thunder, volcanic activity, bolides, avalanches, large animals, and earthquakes, whereas artificial infrasound is mostly generated by powered industrial equipment (Mühlhans, 2017). However, the lower frequency threshold limiting human audible sound levels is not sharply defined at 20 Hz, but depends on the sound pressure. At sufficiently high sound pressure levels, humans can perceive infrasound not only as a hearing sensation, but also as vibrations felt in various parts of the body (Møller and Pedersen, 2004), which differs from the external vibrations of the ground or buildings caused by seismic waves (Rutqvist *et al.*, 2014).

In Helsinki, the simultaneous excitation of ground shaking and sound waves at frequencies around the lower limits of perceptible and audible frequency ranges caused a variety of sensations. These include felt shaking and vibrations, infrasound effects that are difficult to interpret and that result in reports on mixed or combined sensations, and audible effects that are typically described as blasts or thunder-like. Residents navigated to the online macroseismic questionnaire maintained by the Institute of Seismology at the University of Helsinki. Reports in response to an M_L 1.2 event that occurred at 03:50 local time include the following translated statements. "The whole family was awakened by an immense boom, similar to a fierce thunderstorm." "A loud boom was heard indoors." "A rock-based shaking. Lying on the bed it could be heard and felt as a vibration." This statement relates to an M_L 1.0 event at 08:06 local time: "After the boom the movement propagated beneath the feet from the heels to the toes, in north or northeast direction." Quotes from responses to an M_L 1.8 event at 20:35 include "The shaking was felt in the whole house, objects moved on the balcony" and "A sharp metallic bang, no echo. Simultaneously, the apartment shook."

Audible nuisance generated by low-magnitude events prompted the developer to deploy microphone arrays. Flanked by outreach efforts, the general attitude toward the stimulation did not critically decline (Ader *et al.*, 2019), but some reports ("earlier on the same day and during previous days there were similar blasts that were really disturbing") imply that weeks-long exposure to felt and heard disturbances has the potential to negatively impact public opinion on the development stages of geothermal energy production. It has been speculated that resonance effects associated with the Laajalahti Bay are responsible for the sound excitation (Ader *et al.*, 2019). Thus, it seems plausible to expect more sound reports from around the Laajalahti Bay compared to the obtained distribution. However, the resonance hypothesis was ruled out by comparing collocated borehole seismograms and microphone array data (Lamb *et al.*, 2021), which showed that sound typically starts at the onset of the *P* wave (Hill *et al.*, 1976; Tosi *et al.*, 2000), which suggests local excitation. This is compatible with the overall collocated distributions of felt and heard reports, that is, there are no areas with excess reports of audible noise in the absence of reported shaking, which would imply efficient sound propagation. The array data analysis further suggests that later arriving acoustic waves propagating horizontally at the speed of sound are excited by secondary sources associated with the built environment, considering the absence of steep topographic interfaces. The delay here is on the order of a few seconds (Lamb *et al.*, 2021). This implies that secondary sources were located within the epicentral area.

Hillers *et al.* (2020) compare the locations of the obtained reports to the peak amplitudes at the surface of the *P*-wave, *SV*-wave, and *SH*-wave radiation patterns, which are associated with the predominantly thrust-faulting mechanisms of the induced seismicity. Surface waves are not excited by the deep seismicity. Visual inspection of radiation patterns shows good agreement between reporting activity, dominated by the Munkkivuori neighborhood, and the *SH* amplitude distribution in that area. However, the weaker correlation between the *SH* radiation pattern and the locations of the responses to the largest

TABLE 1
Five Investigated Earthquake Source Mechanisms

Event	Event 13	Strike + 90	Dip + 90	Rake + 90	Orthogonal
Strike (°)	328	58	148	328	216
Dip (°)	31	31	59	31	52
Rake (°)	71	71	289	161	91
Focal mechanism plots					

The reference Event 13 is the largest M_L 1.8 event induced during the stimulation that occurred on 16 July 2018 (Hillers *et al.*, 2020). The next three source mechanisms are obtained from the reference event by rotating one angle by 90°. The Orthogonal solution has a slip vector that is orthogonal to the first two mechanisms.

M_L 1.2 event during the 2020 stimulation questions a simple correlation between reporting activity and specific radiation patterns. In this study, we compute the spatial distributions of peak ground velocities and peak sound pressures to analyze the seismoacoustic coupling that is typically associated with the vertical ground motion of *P* waves and *SV* waves (Brissaud *et al.*, 2017, 2021; Averbuch *et al.*, 2020). Our numerical simulations explore the sensitivity of shaking and sound patterns to the properties of the wavefield and the earthquake source. Focusing on scenarios associated with the largest induced M_L 1.8 event in 2018, we address the computational challenges in modeling 3D sound propagation up to 25 Hz. We show that numerical modeling helps to better understand the physical mechanisms that govern the public response to shaking and noise. Our approach can help mitigate seismoacoustic nuisance associated with geothermal stimulation. We discuss but do not quantitatively analyze socioeconomic effects.

NUMERICAL EXPERIMENTS

Earthquake source

We parameterize earthquake point sources at the hypocenter location of the largest M_L 1.8 event that occurred on 16 July 2018 at 17:26:03 UTC. This earthquake was located at 60.196° N, 24.837° E at a depth of 6.1 km. The source mechanism and macroseismic response to this event are detailed in Hillers *et al.* (2020). We convert the local magnitude to the seismic moment following Lund *et al.* (2015) and Kwiatek *et al.* (2019) as

$$M_0 = 10^{(M_L+7.98)/0.83}. \quad (1)$$

We then use a Brune source time function

$$S(t) = \begin{cases} \exp(-(t-t_0)/T)(t-t_0)/T^2 & (t-t_0) > 0 \\ 0 & \text{else} \end{cases}, \quad (2)$$

in which $t_0 = 0.05$ s controls the onset time of seismic moment release, and T = 0.02 s governs the source duration (Brune, 1970; Madariaga, 2011). This results in a seismic point source with a corner frequency of approximately 24 Hz. Specifically, our chosen source time function yields a seismic moment amplitude at 24 Hz, which is a factor of ten smaller than the peak amplitude over the entire frequency range. It is difficult to constrain the kinematics of small earthquakes observationally (Abercrombie, 2021), but relatively short rupture durations in the range of our choice of T = 0.02 s have been reported (e.g., Tomic *et al.*, 2009). We analyze the effects of source geometry on the seismoacoustics using four additional scenario earthquake sources that are obtained by rotating the original moment tensor (Table 1).

Velocity model

Our velocity model includes the solid Earth coupled with a 2-km-thick air or atmospheric layer. Below the ground surface, we use the 1D seismic velocity model of Leonhardt *et al.* (2021) obtained by local vertical seismic profiling. In this model, the velocity increases from ~5.9 km s^{-1} at the surface to ~6.5 km s^{-1} at 3 km depth, and then decreases toward 6 km s^{-1} at 6 km depth. We compute the *S* wavespeed v_S from the available *P* wavespeed v_P using an empirical constant $v_P/v_S = 1.71$ ratio (Leonhardt *et al.*, 2021). We assume a constant density of 2700 kg m^{-3} for the entire domain. For the air layer, we use a constant sound speed $c = 340.5$ m s^{-1} and a constant density $\rho = 1.225$ kg m^{-3}.

The computational mesh

We simulate 3D elastic wave propagation in a domain of 12 km × 12 km × 15 km centered around the source location. The coupled 3D acoustic wave propagation is modeled in the 2 km thick air layer (Fig. 2). At the interface between the elastic and acoustic subdomains, we consider accurate topography data from the National Land Survey of Finland with a resolution of 2 m and interpolate it to the unstructured triangular grid of our surface mesh. The combination of slow sound speed in air and the need to resolve audible frequencies poses a significant computational challenge. To keep the resulting computational cost manageable, we limit the highest resolution area to a cone-shaped refinement region (Fig. 1c). This region includes both the source of the earthquake and the Munkkivuori neighborhood, from where most complaints about sounds were submitted. Inside this region, we set the element sizes to 97 and 14 m for Earth and air, respectively. To enforce a conforming mesh at the elastic–acoustic interface, our mesh contains elastic elements that are nearly as small as the acoustic elements. The topography data further complicate the meshing process and can lead to element sizes much smaller than 14 m in both the elastic

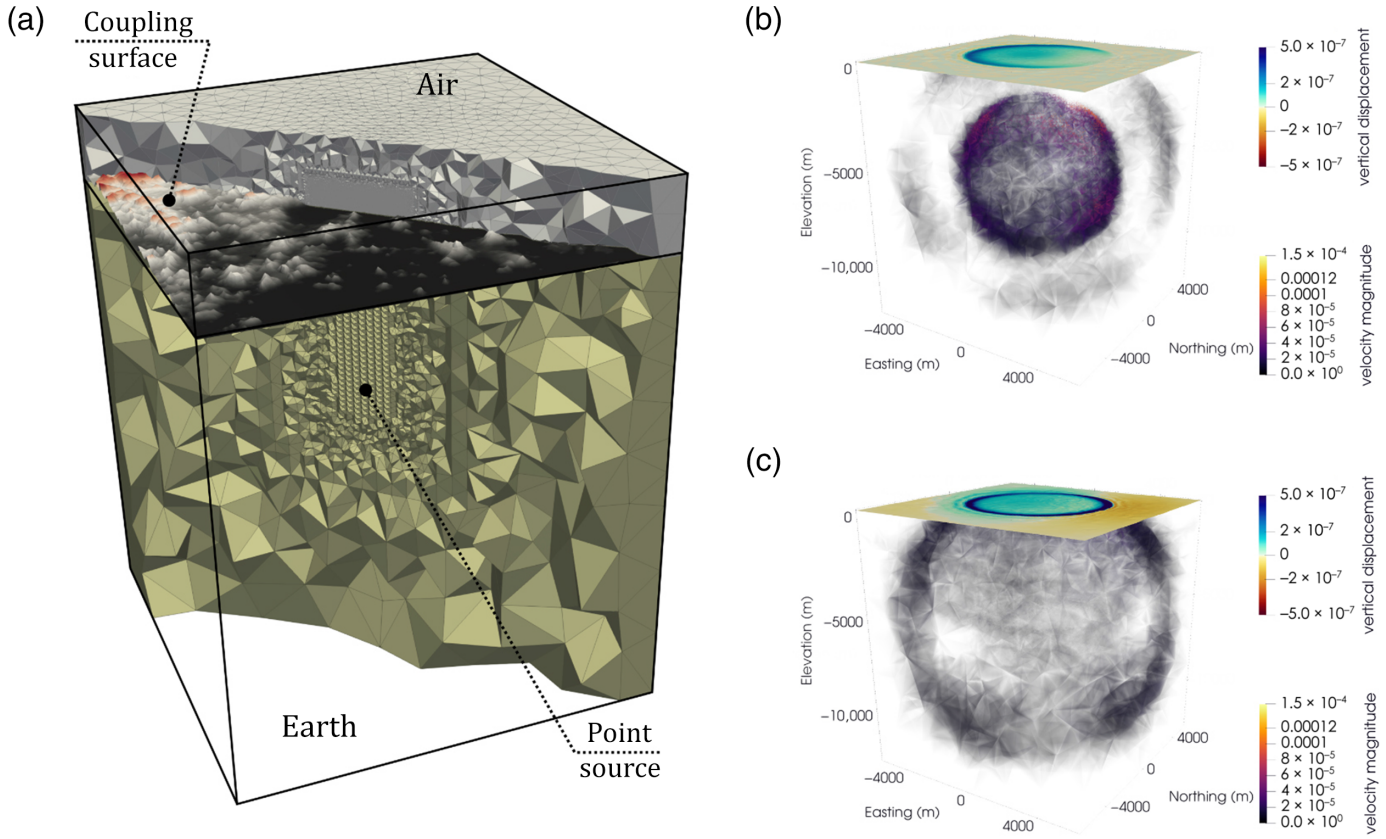

Figure 2. (a) View of our computational mesh with the elastic layer in the lower part and the thinner acoustic layer on top that contains the refined mesh in the central region. We highlight the topography at the interface. (b,c) Velocity field in the volume and vertical displacement at the surface at (b) 1.2 s and (c) 2.0 s for the simulations of event 13, the largest induced earthquake. The *x*-axis points in the west–east direction, the *y*-axis in the north–south direction, and the *z*-axis up–down. The view is from the southeast toward northwest. Note the larger vertical displacement value associated with the *S* wave in panel (c). The color version of this figure is available only in the electronic edition.

and acoustic domains. For example, 1% of all element edges are smaller than 7.04 m. Away from the cone-shaped refinement area at the interface between elastic and acoustic domains, we gradually decrease the mesh resolution to a maximum mesh element size of 2 km. The largest elements serve as cost-effective sponge layers, preventing artificial reflections from imperfect absorbing boundary conditions. Our simulations do not conserve energy because energy is allowed to leave the domain at the absorbing boundaries.

Within each element, we approximate the solution spatially with a fifth-degree polynomial, leading to sixth-order accuracy in space and time (Käser *et al.*, 2008). This subelement resolution allows us to achieve an effective resolution of 2.3 m in air and 16.2 m in Earth within the high-resolution region of interest. The resulting mesh contains 40.9 million elements, of which only 2.6 million correspond to our Earth model. The vast majority of the computational cost stems from the modeling of acoustic wave propagation in air. By employing polynomial basis functions of fifth degree, we obtain 504 degrees of freedom per element. Thus, our mesh includes 20.6 billion degrees of freedom. For comparison, we created a computationally cheaper setup with a uniform mesh resolution of 70 m in the Earth. This setup does not model wave propagation in air and contains 32.5 million elements. Including an air layer with such a high resolution for the entire domain is extremely challenging with the currently available computational infrastructure. We estimate that such a mesh would contain more than 500 million elements and thus more than 250 billion degrees of freedom.

Cluster-based local-time-stepping algorithm

The mesh refinement in the high-resolution region, together with the stark contrast in element size between the elastic and acoustic layers, leads to massive differences in element sizes. Because SeisSol uses an explicit time-integration method for its wave propagation solver, the standard Courant–Friedrichs–Lewy time step restriction (Courant *et al.*, 1928) leads to strongly diverging permissible time step sizes across the elements. To tackle such situations, SeisSol offers a cluster-oriented local-time-stepping (LTS) method that groups elements into clusters according to their admissible time step size (Breuer *et al.*, 2016; Uphoff *et al.*, 2017). Each cluster is updated in a multirate fashion, as often as needed locally. This LTS scheme significantly reduces the time-to-solution of our scenarios and is therefore crucial for the feasibility of our simulations. In our fully coupled scenarios, the minimum time step is 8.4×10^{-6} s. The maximum time step size is 2048

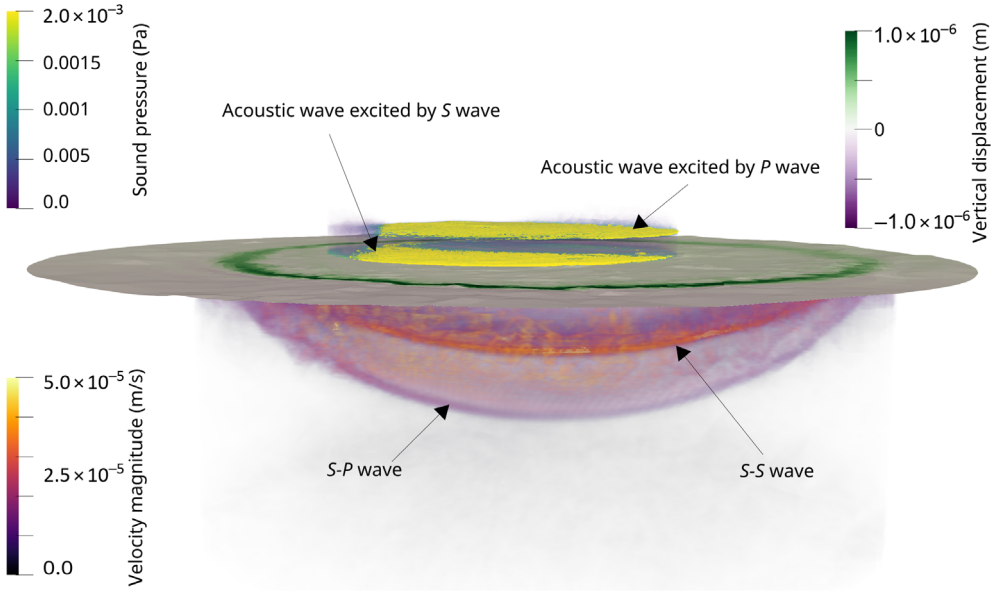

Figure 3. Acoustic and elastic wavefields at $t = 2$ s. The acoustic wavefield is illustrated in a cylinder with 2 km radius around the source, and the seismic wavefield is shown in a 4 km radius. The illustration features two wavefronts in the acoustic layer, the upper one excited by the *P* wave and the lower one excited by the *S* wave. The elastic layer contains the reflected *S* wave (*S*–*S*) and the reflected *P* wave (*S*–*P*) that are both generated by the interaction of the incident *S* wave with the elastic–acoustic interface. The color version of this figure is available only in the electronic edition.

times larger. Our LTS strategy yields an approximate speedup factor of 30 for the fully coupled seismoacoustic model.

Output and postprocessing

Simulated output. In the fully coupled simulations (Fig. 3), we place a grid of receivers within our high-resolution model area with a spacing of 100 m at an elevation of 0.5 m above the free surface to record the synthetic acoustic fields. The seismic wavefield is sampled at receivers located just below the surface at a depth of 0.05 m. The receiver output is written at a sampling rate of 200 times per second. For the Earth-only simulation, we write the velocity and displacement fields at the entire free surface at a rate of 1000 times per second. For a pointwise comparison of recorded data and simulated synthetics, we add receivers at the locations of the four FIN2 acoustic stations (inverted triangle in Fig. 1) from Lamb *et al.* (2021) at 0.5 m elevation. We place approximately 100 seismic receivers at all the locations of the St1 borehole sensors and surface stations of the 2018 HE and OT monitoring networks (Hillers *et al.*, 2020). The triangles in Figure 1 represent the subset used for data comparison. For both the Earth domain-only and coupled simulations, we compute the released energy perturbation at a rate of ten times per second. We visualize the vertical velocity and the velocity magnitude, that is, the length of the velocity vector, recorded at the Earth's surface in Figure 4. Superimposed on the regional topography with maximum elevations on the 10 m scale, these illustrations show source effects, such as the radiation patterns of the *P* wave and *S* wave. We observe the expected smaller *P*-wave amplitudes and path effects associated mainly with topography scattering. Although scattering effects from the topography do not cause strong decoherence of the near-source body-wavefronts, they do cause visible coda arrivals (e.g., Pitarka *et al.*, 2022; Taufiqurrahman *et al.*, 2022). We additionally visualize the 3D volumetric fully coupled wavefields at selected time steps. In Figure 2, we show the magnitude of the velocity wavefield in the volume and vertical displacement at 1.2 s and at 2.0 s. Figure 2b illustrates the four lobes of the *P* wave, which have partially reached the Earth's surface. In the same instance, stronger *S*-wave amplitudes are shown closer to the source. In the later snapshot in Figure 2c, the *P*-wave energy has propagated beyond the computational domain, and the *S* waves start to interact with the Earth's surface. In Figure 3, we illustrate the interaction of the elastic and the acoustic waves at the interface. At 2 s the seismic *P* wave has propagated out of the computational domain, and we only see the reflected *S* wave in the solid Earth. In the atmosphere, we can distinguish two wavefronts that are consecutively excited by the seismic *P* wave and the *S* wave. Hence, although the seismic *P* wave is outside the domain, the corresponding acoustic wave is still propagating inside the computational domain due to the comparatively low sound speed.

Calibration. A commonly used relationship that relates the pressure perturbation ΔP to the vertical ground velocity v is

$$\Delta P = \rho c v, \tag{3}$$

in which ρ is the density of air and c the speed of sound (Cook, 1971; Tosi *et al.*, 2000; Lamb *et al.*, 2021). This result can be obtained by assuming a vertically incident plane wave, which is an exact solution of the acoustic wave equation. Our 3D simulations including topography provide the opportunity to evaluate this approach. For each pair of the 1386 densely spaced elastic and acoustic receivers, we compute the peak ground velocity of the elastic part and the peak pressure perturbation of the acoustic part. We perform a linear regression assuming the following relation:

$$\Delta P^{\text{peak}} = c_0 + c_1 v^{\text{peak}} + \varepsilon, \tag{4}$$

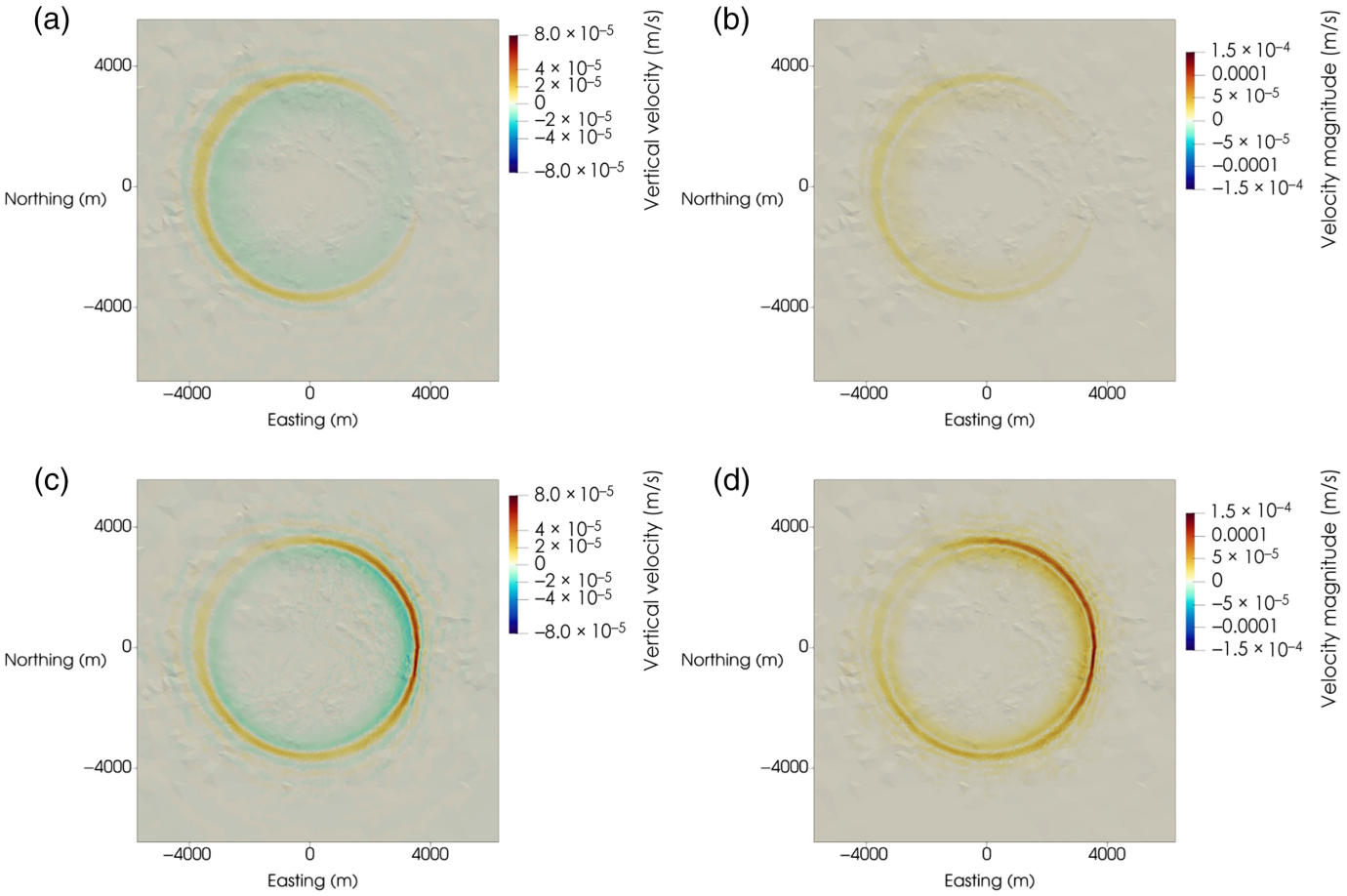

Figure 4. (a,b) Vertical ground velocity and velocity magnitude at 1.2 s for the M_L 1.8 event 13 at the Earth's surface. The timing is associated with the *P* wave. (c,d) Vertical ground velocity and velocity magnitude at 2.0 s. The timing is associated with the *S* wave. The color version of this figure is available only in the electronic edition.

in which ε is a normally distributed error term. The constant factor c_0 is zero if the vertical plane-wave assumption holds. It can be invalidated for reasons such as topography or due to source effects. Here, however, it captures the average difference between the perfectly linear model, given by equation (3), and the measurements. Similarly, we would expect that $c_1 = \rho c \approx 417.1\ \mathrm{kg\,m^{-2}s^{-1}}$.

We implement a workflow that benefits from the combination of our two setups together with this calibrated rule of thumb. First, we simulate the scenario that includes Earth and air. From the refinement zone, we extract the peak ground vertical velocity in the Earth and the sound pressure level in the air. We perform the linear regression equation (4) to obtain the approximate relationship between these two quantities. The result can be interpreted as a calibrated version of equation (3) that considers factors such as topography and vertical and horizontal distance to the source. Next, we compute the refined Earth model without the acoustic coupling, allowing for computational efficiency, and extract the peak vertical ground velocity for the entire domain. Finally, we use the result from the linear regression to estimate the sound pressure level. This combines the strengths of the 3D fully coupled approach with the computational efficiency of the Earth-only approach.

Phase estimation. We investigate whether the *P* wave or the *S* wave has a larger impact on the disturbance patterns. We estimate the arrival time t^S of the *S* wave using the approximate relation $t^S(d) = d/c^S_{\max}$, in which d is the distance to the source and $c^S_{\max} = 3.83\ \mathrm{km\,s^{-1}}$ is the fastest *S* wavespeed in our velocity model. We use this to define the arrival windows. A point with hypocentral distance d is assumed to be affected by the *P* wave at times $t \in (0, c^S_{\max})$ and by the *S* wave for all other times. Because we use a lower bound for the *S*-wave arrival time, we may underestimate the duration of the *P* wave. However, this does not significantly bias our results because the *P* coda amplitudes are smaller than the direct wave amplitudes.

Computational aspects

We ran our setups for 3 s simulated time on the clusters SuperMUC-NG and Mahti. On SuperMUC-NG, our simulations run on 200 nodes with 48 cores per node. The fully

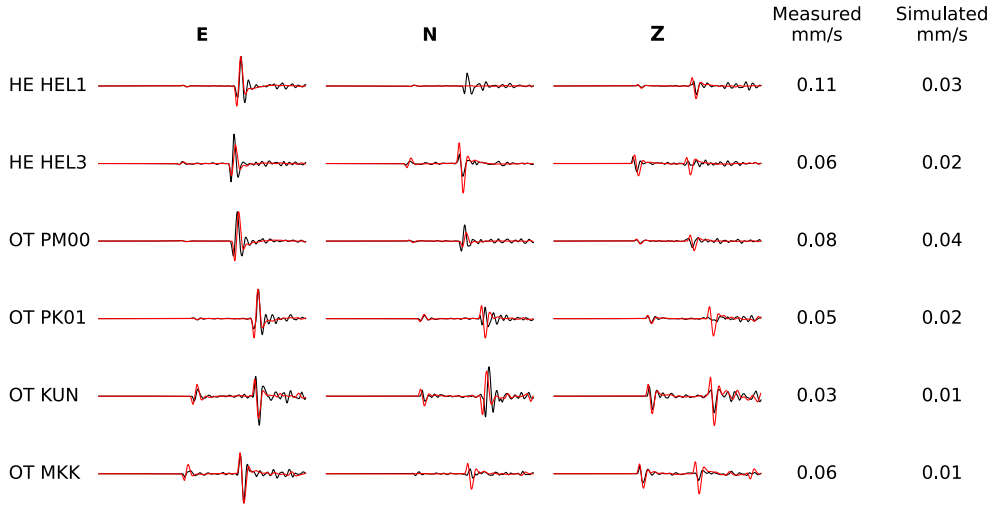

Figure 5. Comparison of 3 s long observed (black) and synthetic (red) velocity waveforms at two broadband and four short-period seismic stations. The HE network stations are permanent broadband sensors, and the four OT network stations are temporary installations of 4.5 Hz geophones connected to CUBE recorders (Hillers *et al.*, 2020). We remove the instrument response from the seismic records using prefilter corner frequencies of 0.5 and 40 Hz considering the band-pass filter range between 1 and 10 Hz applied to all data and synthetics. Synthetic and observed waveforms are aligned with respect to the *P*-wave arrival to account for the arbitrarily chosen onset timing of our source time function. This time shift can vary by 0.02 s between stations. It accounts for velocity heterogeneities that are not included in our 1D velocity model. Synthetic and observed velocity waveforms are normalized individually by the maximum value of the records at each station, that is, we do not normalize waveforms component-wise. The peak velocity is indicated in the last two columns. The color version of this figure is available only in the electronic edition.

coupled model takes about 1.25 hr for one simulation. Simulations on Mahti run with similar efficiency. For a more detailed analysis of the computational efficiency of large-scale fully coupled seismoacoustic simulations with SeisSol, including the local-time-stepping method, we refer to Krenz *et al.* (2021).

RESULTS

Comparison of seismic and acoustic observations and synthetics

We begin the assessment of the synthetics with the comparison of 1–10 Hz filtered three-component seismograms. Figure 5 shows waveforms of the reference M_L 1.8 event at two broadband and four short-period stations located over a wide azimuthal range in the computational domain (triangles in Fig. 1). Together with the relatively low-frequency range, this selection allows us to focus on first-order features, including *P*- and *S*-wave travel time, polarity, and relative *P*- and *S*-wave amplitudes. The visual comparison shows a relatively high consistency for all these characteristics between our synthetic (red) and observed (black) velocity waveforms. Considering the *P*-wave velocities between the surface and the injection depth in the range of 5.9 km s^{-1} to 6.5 km s^{-1}, the overall high quality of the *P*- and *S*-waveform fits, and the relatively small level of scattered waves below 10 Hz, the local geological situation in the southern Fennoscandian Shield on the here considered scales is well approximated by a homogeneous half-space model. Correspondingly, the 1D velocity model obtained at the location of the injection (Leonhardt *et al.*, 2021) in the center of the domain is a good approximation for the 3D velocity structure in the area. The tens-of-meters thick low-velocity layer in the area inferred from an ambient noise surface-wave dispersion analysis (Hillers *et al.*, 2020) does not appear to be relevant for the body-wave propagation below 10 Hz.

The near-perfect consistency of the polarities and the good agreement of the *P*-to-*S* wave ratio between data and synthetics are governed by the source moment tensor properties that have been obtained from first-motion polarity data (Hillers *et al.*, 2020) and from waveform inversion (Rintamäki *et al.*, 2023). The visible inconsistency between data and synthetics such as the *S*-wave properties at the *N* channel of the HEL1, PK01, KUN, and MKK stations suggest, again, a relatively small degree of structural heterogeneity, which is compatible with wave propagation phenomena inferred by array analysis techniques (Taylor *et al.*, 2021; Li *et al.*, 2022).

Similar to the seismogram validation, we also focus on general first-order properties when comparing modeled acoustic time series to acoustic data recorded by the FIN2 microphone array (Lamb *et al.*, 2021). To facilitate the comparison of first-order properties, we consider waveform envelopes (Fig. 6) and spectrograms (Fig. 7). The sensitivity of acoustic data acquisition is demonstrated by the high variability of the recorded time series in Figure 6a. The four sensors were deployed within 80 m distance. We omit simultaneously obtained data from a FIN1 array (Lamb *et al.*, 2021) because of lower data quality. Considering the high intra-array data variability in Figure 6a, the modeled and observed waveform envelopes show an overall good general consistency. The envelopes are not normalized and represented at the same scale. We highlight that the modeled absolute amplitude values of acoustic energy around 0.005 Pa and 0.01 Pa for the *P* wave and *S* wave, respectively (Fig. 6b), fall well within the range of the observed variable

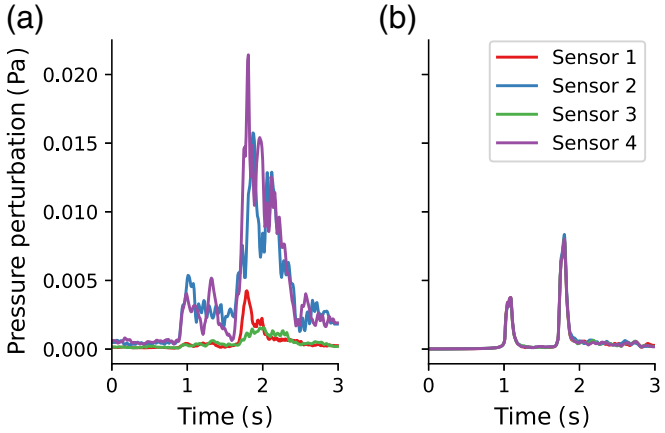

Figure 6. (a) Envelopes of acoustic FIN2 station data (Lamb *et al.*, 2021). The intersensor distance is about 10–30 m. (b) Envelopes of the synthetic acoustic simulation time series. For both observed and simulated data, we apply a 1 Hz high-pass filter and smooth the envelope with a centered moving average filter with a window size of 0.04 s. Colors indicate different stations of the array. The color version of this figure is available only in the electronic edition.

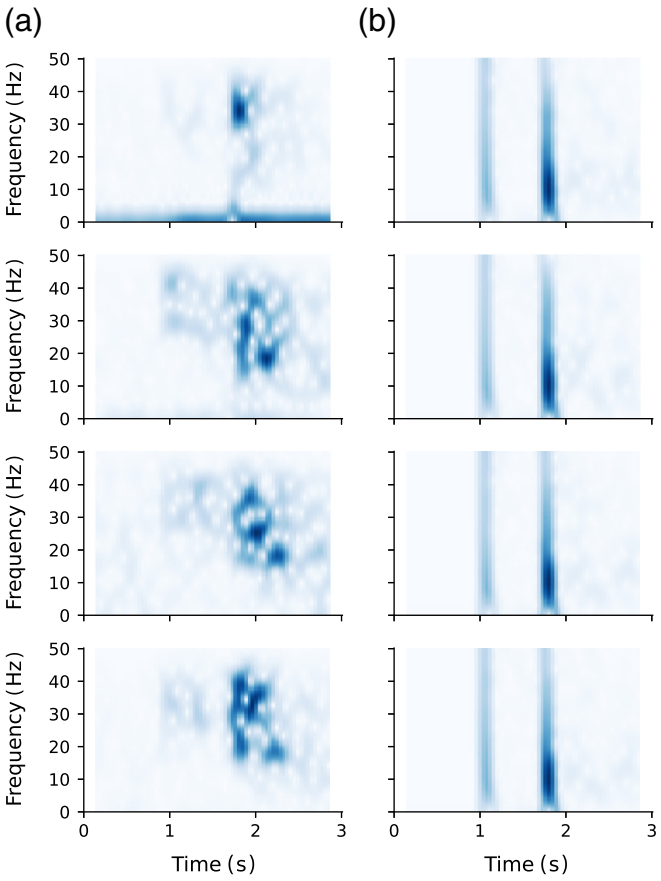

Figure 7. (a) Spectrograms of acoustic signals recorded at the four FIN2 stations computed with a window size of 0.25 s. (b) Synthetic spectrograms downsampled by a factor of two to match the frequency range of the observed data. Accurate numerical resolution is limited to about 25 Hz, and synthetics at higher frequencies may be affected by numerical artifacts. The light and dark colors correspond to weak and strong squared power densities, respectively. The color version of this figure is available only in the electronic edition.

values (Fig. 6a). Again, the variability in the direct *P*-wave and *S*-wave amplitudes between the four records in Figure 6a is larger than the difference between the data average and the synthetics. As for the seismograms, the relative arrival times of the *P*-wave and *S*-wave energy also agree well, which suggests an overall adequate parametrization of the controlling media properties. Both data and synthetics consistently feature higher energy associated with the *S*-wave arrival, which can be understood from the relative station position within the radiation pattern. The strongest systematic disagreement concerns the elevated sound pressure in the coda segments of the *P* wave and *S* wave that is insufficiently reproduced by the numerical simulations.

This pattern of well-resolved timing but deficient coda energy is also displayed in the spectrograms in Figure 7. Acoustic array analysis (e.g., Smink *et al.*, 2019) shows that acoustic coda can be excited by secondary sources associated with the built environment, and it can be affected by propagation effects that can include the scattering of turbulence and reflections off atmospheric boundary layers associated with a temperature inversion. Alternatively, coda waves can be controlled by scattered seismic waves that continue to excite sound locally. Discrimination of the locally governing effects can be supported by the observations of the decreasing high-frequency content with time that is resolved in the spectrograms (Fig. 7a), and by numerical experiments that parameterize inhomogeneities in the subsurface and atmospheric domains.

As for the envelopes, the acoustic spectrograms exhibit similar *S*–*P* times and similarly stronger *S*-wave arrivals. Importantly, however, observed acoustic energy and coda are excited at frequencies that exceed the here accurately modeled frequency range, which is limited to approximately 25 Hz. The high-frequency contributions in the synthetics above 25 Hz are likely affected by numerical dissipation and dispersion errors and noise, for example, as a by-product of the employed high-order scheme that manifests as Gibbs phenomenon (Hesthaven and Warburton, 2008). Hence, despite the successful numerical synthesis of key seismoacoustic wave propagation phenomena at the lower limit of the human audible frequency range, the richness of the acoustic observations at higher frequencies is a reminder of the remaining challenges to modeling the full range of audible earthquake sounds.

Linear regression

We estimate the regression model equation (4), which predicts the peak sound pressure level from the peak vertical surface velocity, for the five different source models individually using the statistical library statsmodels (Seabold and Perktold, 2010).

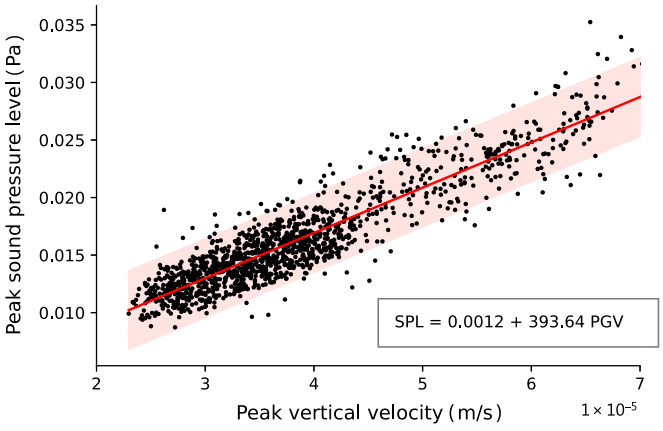

Figure 8. Relationship between the simulated peak ground velocity (PGV) and peak sound pressure level (SPL) inside the high-resolution model refinement zone for the reference M_L 1.8 event 13. We compute this data with our coupled elastic-acoustic simulation. The red line indicates the linear regression fit, and the shaded area is the 95% prediction interval. The color version of this figure is available only in the electronic edition.

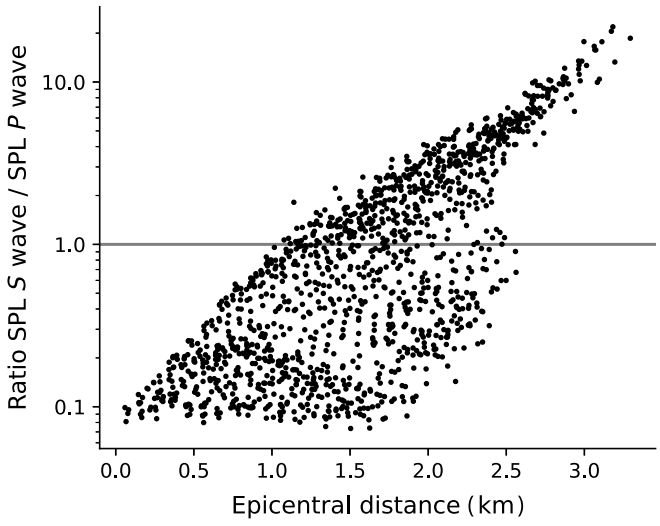

Figure 9. Dependence of the simulated peak sound pressure level ratio on distance. We compute this data with our coupled elastic–acoustic simulation. The *x*-axis indicates the distance to the epicenter. The *y*-axis shows the peak sound pressure level SPL during the passage of *S* waves normalized by the sound pressure level during the *P*-wave passage. The horizontal line at unity indicates balanced SPLs. Values above the line indicate excess SPL of the *S* waves. The values are obtained from the fully coupled simulation for the reference M_L 1.8 event 13 earthquake.

The results are compiled in Table 2. For all simulations, the intercept and slope are statistically significant with $p < 0.001$. The intercept is nonzero for all considered simulations, and the slope is smaller than the prediction equation (3). However, the fit between the model and the synthetics associated with the reference event is good considering the obtained confidence interval and coefficient of determination. With the exception of the Rake + 90 scenario, the other considered rotations of the source moment tensor yield synthetics that show a larger scatter around the model parametrization. In detail, for the reference event, the linear regression results in values of $c_0 = 0.00118 \pm 0.00036$ and $c_1 = 393.64 \pm 9.11$, in which the indicated uncertainty refers to the 95% confidence interval. This model has a coefficient of determination of $r^2 = 0.839$. Compared to equation (3), which leads to a factor of $c_1 \approx 417$, our approximation results in a sound pressure level that is roughly 6% smaller on average. The data and regression results in Figure 8 illustrate the high explanatory power of the linear relationship with only a few outliers. However, it is important to note that a significant number of data points with very-high-sound pressure levels are not predicted well by the linear model. We expect that an even higher resolution in the vicinity of the epicenter, in which high peak ground velocities are simulated, helps to mitigate the remaining mismatches.

TABLE 2
Linear Regression Results

Source	Intercept	Slope	r^2
Event 13	0.00118 ± 0.00036	393.64 ± 9.11	0.839
Strike + 90	0.00243 ± 0.00048	356.22 ± 13.34	0.665
Dip + 90	0.00155 ± 0.00046	381.97 ± 12.30	0.728
Rake + 90	0.00030 ± 0.00019	414.62 ± 7.97	0.883
Orthogonal	0.00265 ± 0.00055	354.70 ± 14.24	0.633

The indicated uncertainty refers to the variation associated with a 95% Student's *t*-test-based confidence interval. The quantity r^2 is the coefficient of determination.

Peak sound pressure of *P* waves and *S* waves

We evaluate the correspondence between the *P* wave and *S* wave and the peak sound level computed by our simulation in the high-resolution area. The *P*-wave is commonly assumed responsible for earthquake sound generation (Hill *et al.*, 1976). To verify this, we use the previously defined *P*-wave and *S*-wave windows (Output and postprocessing section). Using the reference event synthetics, Figure 9 shows that the *P* wave dominates the sound generation at short epicentral distances. The relative contribution of acoustic signals generated by the *S* wave becomes increasingly stronger with distance, and at about 1 km epicentral distance the peak sound pressure is associated with the impinging *S* wave.

Peak ground velocity and sound pressure level distributions

Earlier we presented seismoacoustic results from five fully coupled simulations in the spatially limited high-resolution refinement area (red polygon in Fig. 1). Now we discuss hybrid results obtained using computationally cheaper seismic-only wave propagation simulations in the larger model domain

(black square in Fig. 1), with the sound pressure subsequently estimated using our scaling relation obtained from the high-resolution simulation. For all shaking and sound distributions in Figure 10 we use the Webmercator projection, and we interpolate the simulated data for equidistant spacing. For comparison, we plot the macroseismic response distribution associated with the reference event 13 in the first row of Figure 10. This is a subset of the distribution shown in Figure 1c, in which now the symbols 'x', diamonds and circles indicate heard, felt, and combined disturbances, respectively. The spatial relation is discussed in the Discussion section. Because of our nonperfectly absorbing boundary conditions, we focus on a 8 km × 8 km area in the center of the meshed domain.

The first column of Figure 10 shows distributions of the peak horizontal ground velocity (PGV) using a linear $\mathrm{mm\,s^{-1}}$ scale for all five seismo-acoustic simulations. Peak horizontal seismic ground velocity is a standard quantity in earthquake engineering. In contrast to the assessment of *P*-wave and *S*-wave radiation patterns (Hillers *et al.*, 2020), the PGV values are a better proxy for the impinging seismic wave energy that leads to perceptible ground motions. This is considered to fundamentally govern the public response to shaking. The PGV maps illustrate the variable shaking intensity, and through the connection to the radiation, the PGV patterns are also controlled by the faulting mechanism. The PGV distributions are here, to a smaller degree, modulated by topography, that is, topographic features "light up" in our synthetic shake maps. This includes not only the northwest- to southeast-trending ridge at the northeastern corner of the Laajalahti bay, just south of the Munkkivuori and Munkkiniemi neighborhoods, for the reference M_L 1.8 event (Fig. 10a), but also the hilltops in the southeast of the domain for the Strike + 90 and Orthogonal scenarios.

The second column shows the spatial distribution of the peak sound pressure level SPL in Pascal on a linear scale that is obtained by multiplying the spatially variable peak vertical ground velocity measured along the full synthetic wavetrain with the corresponding proportionality factor estimated in Table 2. These results, too, show a first-order dependence on the focal mechanism with distinct nodal regions of low or no local sound excitation at all. In these nodal areas, the vertical ground velocity is zero; however, the PGV, which corresponds to the horizontal velocity, is not necessarily zero in the same areas.

We isolate the effect of *P*-wave and *S*-wave-induced sound distributions in the third and fourth column of Figure 10 using a linear Pascal scale for the sound pressure level. The *P*-wave and *S*-wave patterns are complementary, regions of relatively high *P*-wave sound energy show low values of *S*-wave noise, and vice versa. However, the choice of column-specific color ranges obscures the comparably weaker *P*-wave sounds. The most intense earthquake sounds are associated with impinging *S* waves.

Most of the resolved source mechanisms of the induced events (Hillers *et al.*, 2020; Leonhardt *et al.*, 2021; Rintamäki *et al.*, 2023) have a very high similarity to the reference M_L 1.8 event 13 mechanism in the first row in Figure 10. In the absence of weak geological zones or structures to accommodate the seismic energy release, the high similarity of the source mechanisms is governed by the fluid-induced response to the ~6 km deep in situ stress conditions in the structurally homogeneous reservoir (Kwiatek *et al.*, 2019). The N110°E direction of the maximum horizontal stress component (Kwiatek *et al.*, 2019) controls the dominating reverse mechanism (Table 1), which is responsible for the predominant shaking pattern during the event sequence. Similarly, the distribution of the SPL peak sound pressure levels in columns two to four are tied to the radiation pattern and hence to the faulting mechanism. The distributions in rows two to five in Figure 10 correspond to alternative scenario focal mechanisms. As said, in the Helsinki case, the source mechanism variability resolved for the largest events is low (Rintamäki *et al.*, 2023), so the scenario results presumably apply only to small events, if any. However, the variability between the scenario PGV results in the first column illustrates that a different stress regime or a different reservoir structure leading to different dominant source mechanisms significantly changes the shaking distribution. For the audible noise estimates, the SPL peak sound pressure values in columns two to four also vary significantly between the different scenarios. This refers to the spatial distribution and to the peak values in the analyzed domain. The Rake + 90 scenario yields similar PGV values compared to the reference event, but the excited sound shown in columns two to four is overall less powerful and hence presumably less annoying for the here considered excitation through coupling across the Earth's surface, compared to the rattling of vertical structures. The results of the scenarios thus highlight the dependence of a geothermal stimulation soundscape on the subsurface response, which may be considered by developers and regulators in addition to the more standard shaking mitigation measures.

Energy

The dominance of the *S* wave for sound generation can also be inferred from the evolution of the acoustic energy perturbation in our simulation. We compute the total acoustic energy perturbation $E(t)$, which is the sum of the acoustic strain energy and the kinematic energy given by

$$E(t) = \int_\Omega \frac{1}{2K} p^2 + \frac{1}{2}\rho \|\boldsymbol{v}\|_2^2 \mathrm{d}\Omega, \tag{5}$$

in which Ω is the total acoustic region, $K = c^2\rho$ is the bulk modulus, and $\|\boldsymbol{v}\|_2^2$ is the squared Euclidean norm of the velocity. We only consider the perturbations in velocity and pressure and ignore the hydrostatic background pressure. Figure 11

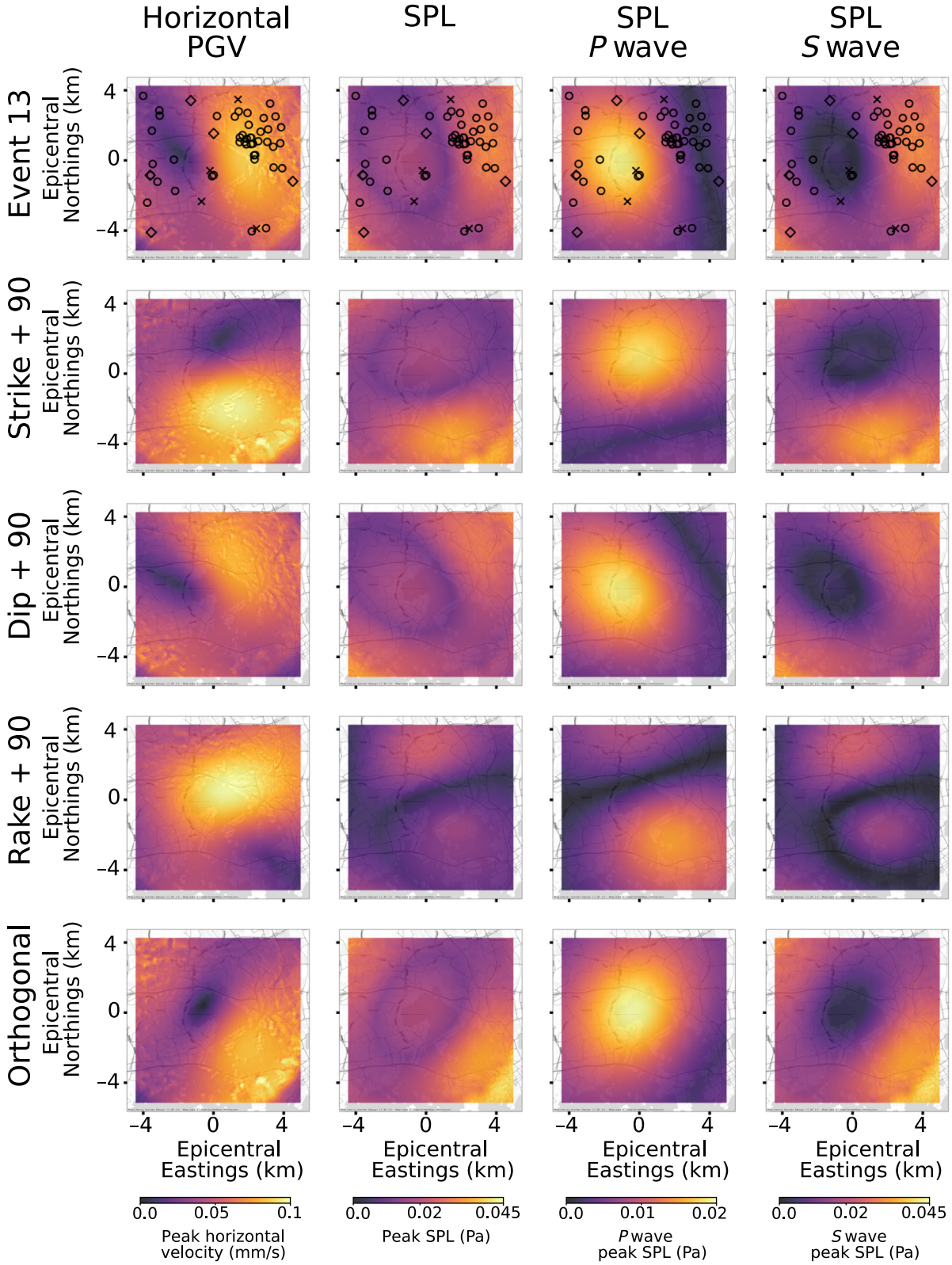

Figure 10. Spatial distributions in the full model domain indicated in Figure 1c of synthetic seismic and acoustic observables of five 3D-coupled simulations using variable source geometries. The markers in the top row indicate observations together with the results associated with the observed M_L 1.8 event mechanism (Hillers *et al.*, 2020). The symbols x, diamonds, and circles indicate audible, shaking, and combined sensations, respectively. The column "Horizontal PGV" shows the peak ground velocity in m s^{-1}. The column "SPL" shows the sound pressure level in Pa, estimated from peak vertical velocity and our calibration routine. The columns "SPL *P* wave" and "SPL *S* wave" show the sound pressure level estimates (in Pa) for the respective wave types. Rows two to five are associated with modified orientations of the original moment tensor point source (Table 1). The color version of this figure is available only in the electronic edition.

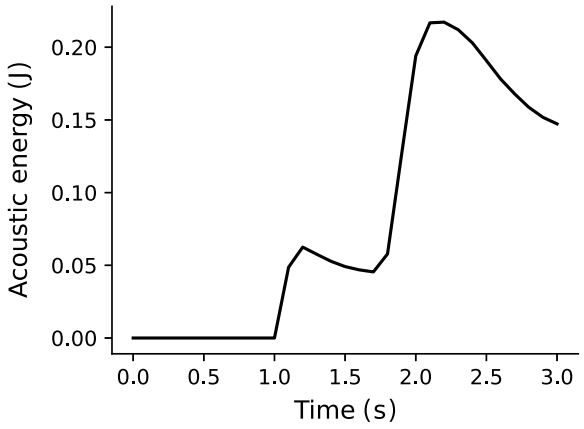

Figure 11. The acoustic energy perturbation for the reference M_L 1.8 event integrated over the air layer indicates that the *S* wave excites more acoustic energy than the *P* wave.

shows the variation of the acoustic energy over time for the reference M_L 1.8 event. Compatible with the data and synthetics in Figures 6 and 7, we observe that the onset of the acoustic energy perturbation coincides with the first arrival of the *P* wave at the free surface. The larger overall increase, however, is associated with the *S*-wave arrival. As the speed of sound in the air is 340.5 $m\,s^{-1}$, acoustic waves begin to leave the 2 km high air layer through the top boundary at about 5.9 s, which is well after our simulation ends. However, acoustic waves can leave the domain through the four lateral boundaries earlier, already during the simulation. Furthermore, the acoustic energy is either converted back to seismic energy or dissipated by SeisSol's specific implementation of the Discontinuous Galerkin method (Dumbser and Käser, 2006). This numerical dissipation stabilizes the method and is smaller in more refined parts of the mesh (Hesthaven and Warburton, 2008).

DISCUSSION

We model the numerically and computationally challenging propagation of coupled seismic and acoustic wavefields in the Helsinki metropolitan area that were excited by stimulated small earthquakes during two EGS development stages. The events triggered in total about 330 macroseismic responses from residents in the neighborhoods in the epicentral area on lateral scales that are similar to the ~6 km depth of the stimulated seismicity. High-quality seismic data and instrumental acoustic observations contribute to this research on the governing factors for irritable sound excitation. Our synthetics are based on variations of the earthquake source corresponding to the largest M_L 1.8 event in 2018. A comparison of these synthetics with seismic and acoustic data demonstrates that the employed 1D velocity model describes the subsurface structure sufficiently accurately and that the stronger local noise excitation from impinging *S* waves compared to *P* waves is a robust feature of the Helsinki stimulation.

The here presented results include frequencies up to 25 Hz, which is at the lower limit of the human audible frequency range. Although we include realistic topography in our model, we omit the water layer in the shallow Laajalahti bay. Including the coupling of acoustic waves across local water bodies poses a considerable meshing challenge (Krenz *et al.*, 2021), and modeling higher frequencies is prohibitively expensive for our available computational resources. In contrast, including low-velocity sedimentary structures that often characterize coastal regions in simulated seismic wave propagation would not noticeably increase the computational load of our approach, which is controlled by the required resolution of acoustic wave propagation in air. The upper crust of the study area in the Fennoscandian Shield is characterized by exceptionally high intrinsic *Q* values (Eulenfeld *et al.*, 2023), hence viscoelastic attenuation effects are negligible. Including attenuation effects in our coupled elastic–acoustic simulations is possible in the future (Uphoff and Bader, 2016) and may be important for the accurate modeling in sediment-rich areas.

We evaluate the assumption that the sound pressure is given by the constant $c\rho$—sound speed times air density—times the vertical ground velocity at the Earth's surface. We fit a linear model to the seismoacoustic synthetics on the refined area (Fig. 1), which allows us to predict the peak sound pressure measured in the air layer from the peak vertical ground velocity in our more refined simulation. Overall, we achieve a good fit for our data for the main event, but our simulated sound excitation tends to be weaker compared to the $c\rho$ scaling factor. The regressions between modeled peak vertical velocity and peak sound pressure show that the sound excitation simulated in our fully coupled seismoacoustic implementation can deviate from commonly employed coupling relations (Tosi *et al.*, 2000; Lamb *et al.*, 2021). The quality of the parameter estimation of the linear scaling relation equation (3) varies between different scenario sources. A likely contributor to the obtained source-geometry dependence (Table 2) is the variable effectiveness of the seismoacoustic coupling that is sensitive to the interaction between radiation patterns and local topography. It is further possible that our underestimation is related to the relatively limited horizontal domain, the steep incidence, and the *S*-wave dominance.

A consistent observation from the available single acoustic data point and from the simulated fields is that the *S* wave excites the strongest audible sound disturbance. This contrasts the typical assumption that the *P* wave dominates sound generation. Again, surface waves were not excited in the region directly above the 6 km deep reservoir. The sample seismic data show that the *S* wave is larger on the horizontal components, but that the vertical motion component that is more relevant for the sound excitation also has a significant amplitude for the *S* wave (Fig. 5). The stronger *S*-wave sound excitation is also demonstrated in the acoustic data. These observations, the synthetics, and the macroseismic reporting activity together

should encourage the deployment of a sufficient number of high-frequency acoustic sensors around future induced seismicity sites. In tandem with other sensor developments such as rotational and six-degrees-of-freedom instruments (Sollberger *et al.*, 2020), or distributed acoustic sensing facilities (Zhan, 2019), more data from more diverse instrumentation can help to better understand the coupled phenomena and the environmental impact of induced earthquakes.

We discuss the spatial relation of the locations of the submitted reports for the largest reference M_L 1.8 event to the computed horizontal PGV shaking proxy and to the acoustic excitation obtained from the vertical component data together with the estimated scaling factor. For this event, nine shaking reports were submitted, 12 on noise, and 62 reported a combination. Figure 10 shows the subset in the epicentral 8 km × 8 km area. The overall PGV distribution is ultimately governed by the radiation pattern for which *P*-wave, *SV*-wave, and *SH*-wave components are considered by Hillers *et al.* (2020). A considerable fraction of the mixed phenomena reports indicated by the circles that dominate the pattern in Figure 10 are located in a low-PGV-value region to the west of the epicenter. Recall that these areas do sustain vertical motion—as indicated by the *P*-wave SPL sound pressure pattern in the third column—that is not captured by the horizontal PGV estimates. The four indicated locations of reported sound sensations (diamonds) and the five 'x' for shaking are insufficient to assess the relations between the excitation and the reporting. Whereas the large PGV values to the northeast suggest a likely connection between the strongest shaking in this area and the observed busiest reporting, the variability in the synthetic PGV and SPL patterns compared to the macroseismic observations implies a more complex relation between excited wavefields and reporting activity.

Tosi *et al.* (2000) surveyed between 500 and 2000 responses to four M_w 5.3–5.8 events that were collected with questionnaires from employees of public authorities within 30 km around the epicenter. The Geographical Society of Finland collected 856 responses from across central Finland following a macroseismic magnitude 4.3 event on 16 November 1931 (Mäntyniemi, 2004, 2017). Close to 900 responses were collected with the Internet questionnaire after an M_L 2.6 earthquake in southern Finland on 19 March 2011 (Mäntyniemi, 2017). This relatively high number is possibly attributed to an intermittently increased public awareness of seismic effects and readiness to share earthquake-related observations, considering that the M_L 2.6 event occurred eight days after the devastating M_w 9.0 Tohoku earthquake, tsunami, and Fukushima nuclear incident. Compared to these cases, the number of 83 reports associated with the largest M_L 1.8 event during the 2018 Helsinki stimulation appears relatively small, which is explained by the correspondingly smaller magnitude. In addition, the spatial distribution of the Helsinki report density varies across the affected area. Thus, it seems premature to infer a single governing mechanism that explains the overall macroseismic report activity from the visual comparison of the synthetic patterns and the felt and heard report locations. The macroseismic observations related to the small-magnitude induced earthquakes in Otaniemi fit the overall experience from macroseismic data related to higher magnitude nondamaging earthquakes.

Macroseismic observations are affected by natural conditions such as the strength of the seismic waves, the soil type and other site effects, characteristics of the building type, and the activity of the respondent at the time of observation. The sensation can vary within a limited area, two neighbors may report quite differently. The reporting activity can be further modulated by controversial social or other factors (Mak and Schorlemmer, 2016; Goltz *et al.*, 2020; Hough and Martin, 2021; Wald, 2021), which is why the connection between our here obtained shaking and noise levels and the perceived and reported nuisance is governed by a set of very diverse variables. The empirical connection between higher socioeconomic status and a higher tendency to report irritable phenomena in the environment, in general, is well documented. Citizens in more affluent areas are typically more active, they have more sociocultural resources, a better understanding of governance practices, and an overall higher level of confidence that they can make a difference (Arnstein, 2019). This suggests that socioeconomic factors can influence—albeit perhaps not control (Wald, 2021)—the response patterns if we consider the reporting of transient, nondamaging environmental disturbances or nuisances as societal participation. In summary, the observed spatial variation in the 2018 Helsinki report density can thus be governed by seismic shaking and acoustic sound effects or, more reasonably, by a combination of these physical and social or socioeconomic effects. Separating the physical from other effects requires the combination of survey data with more data about the physical effects obtained by data acquisition and numerical simulation such as our proposed model. In addition, the survey data could potentially be complemented by building response types and further by comparing the report density and wealth or other relevant socioeconomic indicators in each neighborhood.

CONCLUSIONS

We presented fully coupled elastic–acoustic simulations of seismic and acoustic waves generated by 6 km deep small induced earthquakes in the Helsinki metropolitan area. The computationally expensive simulations of seismic and sound waves across the 12 km × 12 km large epicentral area resolves frequencies around the lower limit of the human hearing sensitivity. Our setup includes realistic material models, topography, and source geometries. We find first-order consistency between our seismic–acoustic simulations and observations. Our results show that shaking and sound patterns correlate with earthquake source mechanisms. Topographic effects

can significantly influence the local acoustic wave excitation, which explains the deviations obtained from commonly applied seismoacoustic coupling relations. The most intense sound in the epicentral area is excited by *S* waves. Our comparison of the simulated seismic and acoustic wave patterns to the macroseismic report locations suggests that reporting activity may be linked to the peak ground velocity distribution. The nuisance related to persistent shaking and noise associated with induced seismicity is a complex sensation that depends on the impinging wavefield properties, environment, and social and personal factors. Together with instrumental and noninstrumental observations, multiphysics simulations can be an important tool to help understand and mitigate the mechanisms that govern public responses to shaking and noise. The obtained relations between shaking and sound and the computational resources needed to synthesize and evaluate the scenario nuisance patterns can inform the planning of future stimulation experiments.

OPEN RESEARCH

Our computational setup is available on Zenodo (https://doi.org/10.5281/zenodo.8056416).

DATA AND RESOURCES

Data from the HE broadband monitoring stations are available through the Institute of Seismology, University of Helsinki. Data from the 2018 temporary installations can be obtained from the GeoForschungsZentrums (GFZ) German Research Centre for Geosciences Data Services (Hillers *et al.*, 2019). Data from the acoustic sensors are proprietary and are not released to the public. We use topography data from the National Land Survey of Finland available at https://www.maanmittauslaitos.fi/ (last accessed April 2021).

DECLARATION OF COMPETING INTERESTS

The authors acknowledge that there are no conflicts of interest recorded.

ACKNOWLEDGMENTS

The authors thank Editor L. Martire and reviewers J. Assink and J. W. Bishop for the comments that helped to improve the article. The authors thank P. Mäntyniemi for curating the macroseismic reports and O. D. Lamb and the St1 team for sharing the acoustic microphone data. G. H. appreciates discussions with P. Mäntyniemi, P. Bäcklund, and V. Bernelius on factors relevant to citizen participation. This work is supported by an Academy of Finland grant, Decision Number 337913. The 2018 temporary deployments were supported by the Geophysical Instrument Pool Potsdam under Grant Number 201802. L. K., S. W., A. A. G., and M. B. acknowledge funding provided (as part of the EuroHPC Joint Undertaking) for the ChEESE-2P cluster of excellence by Horizon Europe (Grant Agreement Number 1010930) and by the German Ministry of Research and Education. S. W. and M. B. acknowledge funding from the Competence Network for Scientific High-Performance Computing in Bavaria (KONWIHR). A. A. G. acknowledges funding from the European Union's Horizon 2020 research and innovation program (TEAR, Grant Agreement Number 852992) and Horizon Europe (DT-Geo, Grant Agreement Number 101058129 and Geo-Inquire, Grant Agreement Number 101058518), as well as the National Science Foundation under NSF EAR-2121666 and the National Aeronautics and Space Administration under 80NSSC20K0495. The CSC IT Center for Science, Finland, grand challenge Project Number 2003841 provided access to the CSC Mahti computational infrastructure. The authors acknowledge resources provided by the Gauss Centre for Supercomputing e.V. available at www.gauss-centre.eu on SuperMUC-NG at the Leibniz Supercomputing Centre available at www.lrz.de, project pr83no. The authors use the Python library contextily for the background maps. The background map tiles were obtained from OpenStreet maps, Stamen Design, and CARTO. The Stamen map tiles are licensed under CC BY 3.0. Data by OpenStreetMap, under ODbL. Refer to openstreetmap.org/copyright for more details. All websites were last accessed in June 2023.

REFERENCES

Abercrombie, R. E. (2021). Resolution and uncertainties in estimates of earthquake stress drop and energy release, *Phil. Trans. Roy. Soc. Lond. A* **379,** no. 2196, doi: 10.1098/rsta.2020.0131.

Abrahams, L. S., L. Krenz, E. M. Dunham, A. A. Gabriel, and T. Saito (2023). Comparison of methods for coupled earthquake and tsunami modelling, *Geophys. J. Int.* **234,** no. 1, 404–426, doi: 10.1093/gji/ggad053.

Ader, T., M. Chendorain, M. Free, T. Saarno, P. Heikkinen, P. E. Malin, P. Leary, G. Kwiatek, G. Dresen, F. Bluemle, and T. Vuorinen (2019). Design and implementation of a traffic light system for deep geothermal well stimulation in Finland, *J. Seismol.* **24,** no. 5, 991–1014, doi: 10.1007/s10950-019-09853-y.

Arnstein, S. R. (2019). A ladder of citizen participation, *J. Am. Inst. Plann.* **85,** no. 1, 24–34, doi: 10.1080/01944363.2018.1559388.

Arrowsmith, S. J., J. B. Johnson, D. P. Drob, and M. A. H. Hedlin (2010). The seismoacoustic wavefield: A new paradigm in studying geophysical phenomena, *Rev. Geophys.* **48,** no. 4, doi: 10.1029/2010RG000335.

Averbuch, G., J. D. Assink, and L. G. Evers (2020). Long-range atmospheric infrasound propagation from subsurface sources, *J. Acoust. Soc. Am.* **147,** no. 2, 1264–1274, doi: 10.1121/10.0000792.

Baisch, S., C. Koch, and A. Muntendam-Bos (2019). Traffic light systems: To what extent can induced seismicity be controlled? *Seismol. Res. Lett.* **90,** no. 3, 1145–1154, doi: 10.1785/0220180337.

Bentz, S., G. Kwiatek, P. Martínez-Garzón, M. Bohnhoff, and G. Dresen (2020). Seismic moment evolution during hydraulic stimulations, *Geophys. Res. Lett.* **47,** no. 5, e2019GL086185, doi: 10.1029/2019GL086185.

Bommer, J. J., S. Oates, J. M. Cepeda, C. Lindholm, J. Bird, R. Torres, G. Marroquín, and J. Rivas (2006). Control of hazard due to seismicity induced by a hot fractured rock geothermal project, *Eng. Geol.* **83,** no. 4, 287–306, doi: 10.1016/j.enggeo.2005.11.002.

Bommer, J. J., P. J. Stafford, B. Edwards, B. Dost, E. van Dedem, A. Rodriguez-Marek, P. Kruiver, J. van Elk, D. Doornhof, and M. Ntinalexis (2017). Framework for a ground-motion model for induced seismic hazard and risk analysis in the Groningen gas field, The Netherlands, *Earthq. Spectra* **33,** no. 2, 481–498, doi: 10.1193/082916EQS138M.

Breuer, A., A. Heinecke, and M. Bader (2016). Petascale local time stepping for the ADER-DG finite element method, *2016 IEEE*

International Parallel and Distributed Processing Symposium (IPDPS), 23–27 May 2016, Chicago, Illinois, U.S.A., 854–863, doi: 10.1109/IPDPS.2016.109.

Brissaud, Q., S. Krishnamoorthy, J. M. Jackson, D. C. Bowman, A. Komjathy, J. A. Cutts, Z. Zhan, M. T. Pauken, J. S. Izraelevitz, and G. J. Walsh (2021). The first detection of an earthquake from a balloon using its acoustic signature, *Geophys. Res. Lett.* **48,** no. 12, doi: 10.1029/2021gl093013.

Brissaud, Q., R. Martin, R. F. Garcia, and D. Komatitsch (2017). Hybrid Galerkin numerical modelling of elastodynamics and compressible Navier-Stokes couplings: Applications to seismo-gravito acoustic waves, *Geophys. J. Int.* **210,** no. 2, 1047–1069, doi: 10.1093/gji/ggx185.

Brooks, E. M., S. Stein, B. D. Spencer, L. Salditch, M. D. Petersen, and D. E. McNamara (2018). Assessing earthquake hazard map performance for natural and induced seismicity in the central and eastern United States, *Seismol. Res. Lett.* **89,** no. 1, 118–126.

Brune, J. N. (1970). Tectonic stress and the spectra of seismic shear waves from earthquakes, *J. Geophys. Res.* **75,** no. 26, 4997–5009, doi: 10.1029/JB075i026p04997.

Che, I. Y., K. Kim, A. Le Pichon, J. Park, S. Arrowsmith, and B. Stump (2022). Illuminating the North Korean nuclear explosion test in 2017 using remote infrasound observations, *Geophys. J. Int.* **228,** no. 1, 308–315, doi: 10.1093/gji/ggab338.

Cook, R. K. (1971). Infrasound radiated during the Montana earthquake of 1959 August 18, *Geophys. J. Int.* **26,** nos. 1/4, 191–198, doi: 10.1111/j.1365-246X.1971.tb03393.x.

Courant, R., K. Friedrichs, and H. Lewy (1928). Über die partiellen Differenzengleichungen der mathematischen Physik, *Mathematische Annalen* **100,** no. 1, 32–74, doi: 10.1007/BF01448839 (in German).

Davison, C. (1938). Earthquake sounds, *Bull. Seismol. Soc. Am.* **28,** no. 3, 147–161, doi: 10.1785/BSSA0280030147.

Dumbser, M., and M. Käser (2006). An arbitrary high-order discontinuous Galerkin method for elastic waves on unstructured meshes - II. The three-dimensional isotropic case, *Geophys. J. Int.* **167,** no. 1, 319–336, doi: 10.1111/j.1365-246X.2006.03120.x.

Ebel, J. E., V. Vudler, and M. Celata (1982). The 1981 microearthquake swarm near Moodus, Connecticut, *Geophys. Res. Lett.* **9,** no. 4, 397–400, doi: 10.1029/GL009i004p00397.

Edwards, W. N., C. D. de Groot-Hedlin, and M. A. H. Hedlin (2014). Forensic investigation of a probable meteor sighting using USArray acoustic data, *Seismol. Res. Lett.* **85,** no. 5, 1012–1018, doi: 10.1785/0220140056.

Eulenfeld, T., G. Hillers, T. A. T. Vuorinen, and U. Wegler (2023). Induced earthquake source parameters, attenuation, and site effects from waveform envelopes in the fennoscandian shield, *J. Geophys. Res.* **128,** no. 4, e2022JB025162, doi: 10.1029/2022JB025162.

Evers, L. G., D. Brown, K. D. Heaney, J. D. Assink, P. S. M. Smets, and M. Snellen (2014). Evanescent wave coupling in a geophysical system: Airborne acoustic signals from the Mw 8.1 Macquarie Ridge earthquake, *Geophys. Res. Lett.* **41,** no. 5, 1644–1650, doi: 10.1002/2013GL058801.

Fastl, H., and E. Zwicker (2006). *Psychoacoustics: Facts and Models*, Vol. 22, Springer Science & Business Media, doi: 10.1007/978-3-540-68888-4.

Galis, M., J. P. Ampuero, P. M. Mai, and F. Cappa (2017). Induced seismicity provides insight into why earthquake ruptures stop, *Sci. Adv.* **3,** no. 12, eaap7528, doi: 10.1126/sciadv.aap7528.

Gaucher, E., M. Schoenball, O. Heidbach, A. Zang, P. A. Fokker, J. D. van Wees, and T. Kohl (2015). Induced seismicity in geothermal reservoirs: A review of forecasting approaches, *Renew. Sustain. Energy Rev.* **52,** 1473–1490, doi: 10.1016/j.rser.2015.08.026.

Goltz, J. D., H. Park, G. Nakano, and K. Yamori (2020). Earthquake ground motion and human behavior: Using DYFI data to assess behavioral response to earthquakes, *Earthq. Spectra* **36,** no. 3, 1231–1253.

Grigoli, F., S. Cesca, E. Priolo, A. P. Rinaldi, J. F. Clinton, T. A. Stabile, B. Dost, M. G. Fernandez, S. Wiemer, and T. Dahm (2017). Current challenges in monitoring, discrimination, and management of induced seismicity related to underground industrial activities: A European perspective, *Rev. Geophys.* **55,** no. 2, 310–340, doi: 10.1002/2016RG000542.

Häring, M. O., U. Schanz, F. Ladner, and B. C. Dyer (2008). Characterisation of the Basel 1 enhanced geothermal system, *Geothermics* **37,** 469–495, doi: 10.1016/j.geothermics.2008.06.002.

Hedlin, M., K. Walker, D. Drob, and C. de Groot-Hedlin (2012). Infrasound: Connecting the solid earth, oceans, and atmosphere, *Annu. Rev. Earth Planet. Sci.* **40,** no. 327, 2012, doi: 10.1146/annurev-earth-042711-105508.

Hernandez, B., A. Le Pichon, J. Vergoz, P. Herry, L. Ceranna, C. Pilger, E. Marchetti, M. Ripepe, and R. Bossu (2018). Estimating the ground-motion distribution of the 2016 Mw 6.2 Amatrice, Italy, earthquake using remote infrasound observations, *Seismol. Res. Lett.* **89,** no. 6, 2227–2236, doi: 10.1785/0220180103.

Hesthaven, J. S., and T. Warburton (2008). *Nodal Discontinuous Galerkin Methods: Algorithms, Analysis, and Applications, Texts in Applied Mathematics*, Springer-Verlag, New York, doi: 10.1007/978-0-387-72067-8.

Hill, D. P. (2011). What is that mysterious booming sound? *Seismol. Res. Lett.* **82,**no. 5, 619–622, doi: 10.1785/gssrl.82.5.619.

Hill, D. P., F. G. Fischer, K. M. Lahr, and J. M. Coakley (1976). Earthquake sounds generated by body-wave ground motion, *Bull. Seismol. Soc. Am.* **66,** no. 4, 1159–1172.

Hillers, G., T. A. T. Vuorinen, E. J. Arola, V. E. Katajisto, M. P. Koskenniemi, B. M. McKevitt, S. Rezaei, L. A. Rinne, I. E. Salmenperä, P. J. Seipäjärvi, *et al.* (2019). A 100 3-component sensor deployment to monitor the 2018 EGS stimulation in Espoo/Helsinki, southern Finland - Datasets, doi: 10.5880/GIPP.201802.1.

Hillers, G., T. A. T. Vuorinen, M. R. Uski, J. T. Kortström, P. B. Mäntyniemi, T. Tiira, P. E. Malin, and T. Saarno (2020). The 2018 geothermal reservoir stimulation in Espoo/Helsinki, southern Finland: Seismic network anatomy and data features, *Seismol. Res. Lett.* doi: 10.1785/0220190253.

Holmgren, J. M., G. Kwiatek, and M. J. Werner (2023). Nonsystematic rupture directivity of geothermal energy induced microseismicity in Helsinki, Finland, *J. Geophys. Res.* **128,** no. 3, e2022JB025226, doi: 10.1029/2022JB025226.

Hough, S. E., and S. S. Martin (2021). Which earthquake accounts matter? *Seismol. Res. Lett.* **92,** no. 2A, 1069–1084, doi: 10.1785/0220200366.

Hupe, P., L. Ceranna, A. Le Pichon, R. S. Matoza, and P. Mialle (2022). International Monitoring System infrasound data products for atmospheric studies and civilian applications, *Earth Syst. Sci. Data* **14,** no. 9, 4201–4230, doi: 10.5194/essd-14-4201-2022.

Käser, M., V. Hermann, and Puente J. D. L. (2008). Quantitative accuracy analysis of the discontinuous Galerkin method for seismic wave propagation, *Geophys. J. Int.* **173,** no. 3, 990–999, doi: 10.1111/j.1365-246X.2008.03781.x.

Keil, S., J. Wassermann, and T. Megies (2022). Estimation of ground motion due to induced seismicity at a geothermal power plant near Munich, Germany, using numerical simulations, *Geothermics* **106,** 102,577.

Krenz, L., C. Uphoff, T. Ulrich, A. A. Gabriel, L. S. Abrahams, E. M. Dunham, and M. Bader (2021). 3D acoustic-elastic coupling with gravity: The dynamics of the 2018 Palu, Sulawesi earthquake and tsunami, *Proc. of the International Conf. for High Performance Computing, Networking, Storage and Analysis*, 1–14, doi: 10.1145/3458817.3476173.

Kwiatek, G., P. Martinez Garzon, J. Davidsen, P. Malin, A. Karjalainen, M. Bohnhoff, and G. Dresen (2022). Limited earthquake interaction during a geothermal hydraulic stimulation in Helsinki, Finland, *J. Geophys. Res.* **127,** no. 9, doi: 10.1029/2022JB024354.

Kwiatek, G., T. Saarno, T. Ader, F. Bluemle, M. Bohnhoff, M. Chendorain, G. Dresen, P. Heikkinen, I. Kukkonen, P. Leary, *et al.* (2019). Controlling fluid-induced seismicity during a 6.1-km-deep geothermal stimulation in Finland, *Sci. Adv.* **5,** no. 5, eaav7224, doi: 10.1126/sciadv.aav7224.

Lamb, O. D., J. M. Lees, P. E. Malin, and T. Saarno (2021). Audible acoustics from low-magnitude fluid-induced earthquakes in Finland, *Sci. Rep.* **11,** no. 1, 1–8, doi: 10.1038/s41598-021-98701-6.

Lecoulant, J., C. Guennou, L. Guillon, and J. Y. Royer (2019). Three-dimensional modeling of earthquake generated acoustic waves in the ocean in simplified configurations, *J. Acoust. Soc. Am.* **146,** no. 3, 2113–2123, doi: 10.1121/1.5126009.

Leonhardt, M., G. Kwiatek, P. Martínez-Garzón, M. Bohnhoff, T. Saarno, P. Heikkinen, and G. Dresen (2021). Seismicity during and after stimulation of a 6.1km deep enhanced geothermal system in Helsinki, Finland, *Eur. Geosci. Union* **12,** no. 3, 581–594, doi: 10.5194/se-12-581-2021.

Li, B., A. A. Gabriel, A. Rintamäki, and G. Hillers (2021). Array based analysis of induced earthquake characteristics using beamforming and back-projection methods in Helsinki, Finland, *EGU General Assembly Conference Abstracts*, EGU21–12888, doi: 10.5194/egusphere-egu21-12888.

Li, B., B. Wu, H. Bao, D. D. Oglesby, A. Ghosh, A. A. Gabriel, L. Meng, and R. Chu (2022). Rupture heterogeneity and directivity effects in back-projection analysis, *J. Geophys. Res.* **127,** no. 3, e2021JB022663, doi: 10.1029/2021JB022663.

Lund, B., M. Malm, P. Mäntyniemi, K. Oinonen, T. Tiira, M. Uski, and T. Vuorinen (2015). *Evaluating Seismic Hazard for the Hanhikivi Nuclear Power Plant Site, Seismological Characteristics of the Source Areas, Attenuation of Seismic Signal, and Probabilistic Analysis of Seismic Hazard*, Volume Rept. NE-4459, ÅF-Consult Ltd., Finland.

Madariaga, R. (2011). Earthquake scaling laws, in *Extreme Environmental Events*,R. A. Meyers (Editor), Springer New York, New York, 364–383, doi: 10.1007/978-1-4419-7695-6_22.

Majer, E., J. Nelson, A. Robertson-Tait, J. Savy, and I. Wong (2012). Protocol for addressing induced seismicity associated with enhanced geothermal systems, U.S. Department of Energy, 52 pp.

Mak, S., and D. Schorlemmer (2016). What makes people respond to "Did You Feel It"?, *Seismol. Res. Lett.* **87,** no. 1, 119–131, doi: 10.1785/0220150056.

Mäntyniemi, P. B. (2004). Pre-instrumental earthquakes in a low-seismicity region: A reinvestigation of the macroseismic data for the 16 November 1931 events in Central Finland using statistical analysis, *J. Seismol.* **8,** no. 1, 71–90, doi: 10.1023/B:JOSE.0000009501.13091.2d.

Mäntyniemi, P. B. (2017). Macroseismology in Finland from the 1730s to the 2000s. Part 2: From an obligation of the learned elite to citizen science, *Geophysica* **52,** 23–41.

Mäntyniemi, P. B. (2022). Revisiting Svenskby, southeastern Finland: Communications regarding low-magnitude earthquakes in 1751–1752, *Geosciences* **12,** no. 9, doi: 10.3390/geosciences12090338.

Megies, T., and J. Wassermann (2014). Microseismicity observed at a non-pressure-stimulated geothermal power plant, *Geothermics* **52,** 36–49, doi: 10.1016/j.geothermics.2014.01.002.

Mignan, A., M. Broccardo, S. Wiemer, and D. Giardini (2017). Induced seismicity closed-form traffic light system for actuarial decision-making during deep fluid injections, *Sci. Rep.* **7,** no. 1, 1–10, doi: 10.1038/s41598-017-13585-9.

Møller, H., and C. S. Pedersen (2004). Hearing at low and infrasonic frequencies, *Noise Health* **6,** no. 23, 37–57.

Mühlhans, J. H. (2017). Low frequency and infrasound: A critical review of the myths, misbeliefs and their relevance to music perception research, *Musicae Scientiae* **21,** no. 3, 267–286, doi: 10.1177/1029864917690931.

Mutschlecner, J. P., and R. W. Whitaker (2005). Infrasound from earthquakes, *J. Geophys. Res.* **110,** no. D1, 1–11, doi: 10.1029/2004JD005067.

Pitarka, A., A. Akinci, P. De Gori, and M. Buttinelli (2022). Deterministic 3D ground-motion simulations (0–5 Hz) and surface topography effects of the 30 October 2016 Mw6.5 Norcia, Italy, earthquake, *Bull. Seismol. Soc. Am.* **112,** no. 1, 262–286, doi: 10.1785/0120210133.

Rintamäki, A., G. Hillers, S. Heimann, T. Dahm, and A. Korja (2023). Centroid full moment tensor analysis reveals fluid channels opened by induced seismicity at EGS, Helsinki region, southern Finland, *EGU General Assembly Conference Abstracts*, EGU23–12756, doi: 10.5194/egusphere-egu23-12756.

Rintamäki, A. E., G. Hillers, T. A. T. Vuorinen, T. Luhta, J. M. Pownall, C. Tsarsitalidou, K. Galvin, J. Keskinen, J. T. Kortström, T. C. Lin, *et al.* (2021). A seismic network to monitor the 2020 EGS stimulation in the Espoo/Helsinki area, southern Finland, *Seismol. Res. Lett.* **93,** no. 2A, 1046–1062, doi: 10.1785/0220210195.

Rutqvist, J., F. Cappa, A. P. Rinaldi, and M. Godano (2014). Modeling of induced seismicity and ground vibrations associated with geologic CO2 storage, and assessing their effects on surface structures and human perception, *Int. J. Greenhouse Gas Control* **24,** 64–77, doi: 10.1016/j.ijggc.2014.02.017.

Schultz, R., G. C. Beroza, and W. L. Ellsworth (2021). A risk-based approach for managing hydraulic fracturing–induced seismicity, *Science* **372,** no. 6541, 504–507, doi: 10.1126/science.abg5451.

Schultz, R., V. Quitoriano, D. J. Wald, and G. C. Beroza (2021). Quantifying nuisance ground motion thresholds for induced

earthquakes, *Earthq. Spectra* **37,** no. 2, 789–802, doi: 10.1177/8755293020988025.

Seabold, S., and J. Perktold (2010). Statsmodels: Econometric and statistical modeling with Python, *9th Python in Science Conference*, doi: 10.25080/Majora-92bf1922-011.

Shani-Kadmiel, S., G. Averbuch, P. Smets, J. Assink, and L. Evers (2021). The 2010 Haiti earthquake revisited: An acoustic intensity map from remote atmospheric infrasound observations, *Earth Planet. Sci. Lett.* **560,** 116,795, doi: 10.1016/j.epsl.2021.116795.

Smink, M. M. E., J. D. Assink, F. C. Bosveld, P. S. M. Smets, and L. G. Evers (2019). A three-dimensional array for the study of infrasound propagation through the atmospheric boundary layer, *J. Geophys. Res.* **124,** no. 16, 9299–9313, doi: 10.1029/2019JD030386.

Sollberger, D., H. Igel, C. Schmelzbach, P. Edme, D. J. van Manen, F. Bernauer, S. Yuan, J. Wassermann, U. Schreiber, and J. O. A. Robertsson (2020). Seismological processing of six degree-of-freedom ground-motion data, *Sensors* **20,** no. 23, doi: 10.3390/s20236904.

Stauffacher, M., N. Muggli, A. Scolobig, and C. Moser (2015). Framing deep geothermal energy in mass media: The case of Switzerland, *Technol. Forecast. Soc. Change* **98,** 60–70, doi: 10.1016/j.techfore.2015.05.018.

Sylvander, M., and D. G. Mogos (2005). The sounds of small earthquakes: Quantitative results from a study of regional macroseismic bulletins, *Bull. Seismol. Soc. Am.* **95,** no. 4, 1510–1515, doi: 10.1785/0120040197.

Sylvander, M., C. Ponsolles, S. Benahmed, and J. F. Fels (2007). Seismoacoustic recordings of small earthquakes in the Pyrenees: Experimental results, *Bull. Seismol. Soc. Am.* **97,** no. 1B, 294–304, doi: 10.1785/0120060009.

Taufiqurrahman, T., A. A. Gabriel, T. Ulrich, L. Valentova, and F. Gallovič (2022). Broadband dynamic rupture modeling with fractal fault roughness, frictional heterogeneity, viscoelasticity and topography: The 2016 Mw 6.2 Amatrice, Italy earthquake, *Geophys. Res. Lett.* **49,** no. 22, doi: 10.1029/2022GL098872.

Taylor, G., G. Hillers, and T. A. T. Vuorinen (2021). Using array-derived rotational motion to obtain local wave propagation properties from earthquakes induced by the 2018 geothermal stimulation in Finland, *Geophys. Res. Lett.* **48,** no. 6, e2020GL090403, doi: 10.1029/2020GL090403.

Thouvenot, F., L. Jenatton, and J. P. Gratier (2009). 200-m-deep earthquake swarm in Tricastin (lower Rhne Valley, France) accounts for noisy seismicity over past centuries, *Terra Nova* **21,** no. 3, 203–210, doi: 10.1111/j.1365-3121.2009.00875.x.

Tomic, J., R. Abercrombie, and A. Do Nascimento (2009). Source parameters and rupture velocity of small M≤2.1 reservoir induced earthquakes, *Geophys. J. Int.* **179,** no. 2, 1013–1023, doi: 10.1111/j.1365-246X.2009.04233.x.

Tosi, P., V. De Rubeis, A. Tertulliani, and C. Gasparini (2000). Spatial patterns of earthquake sounds and seismic source geometry, *Geophys. Res. Lett.* **27,** no. 17, 2749–2752, doi: 10.1029/2000GL011377.

Ulrich, T., A. A. Gabriel, and E. H. Madden (2022). Stress, rigidity and sediment strength control megathrust earthquake and tsunami dynamics, *Nature Geosci.* **15,** no. 1, 67–73, doi: 10.1038/s41561-021-00863-5.

Uphoff, C., and M. Bader (2016). Generating high performance matrix kernels for earthquake simulations with viscoelastic attenuation, *2016 International Conf. on High Performance Computing and Simulation (HPCS)*, IEEE, 908–916, doi: 10.1109/HPCSim.2016.7568431.

Uphoff, C., S. Rettenberger, M. Bader, E. H. Madden, T. Ulrich, S. Wollherr, and A. A. Gabriel (2017). Extreme scale multi-physics simulations of the tsunamigenic 2004 Sumatra megathrust earthquake, *Proc. of the International Conference for High Performance Computing, Networking, Storage and Analysis, SC '17*, ACM, New York, NY, U.S.A, 21:1–21:16, doi: 10.1145/3126908.3126948, event-place: Denver, Colorado.

Uski, M., and A. Tuppurainen (1996). A new local magnitude scale for the Finnish seismic network, *Tectonophysics* **261,** nos. 1/3, 23–37, doi: 10.1016/0040-1951(96)00054-6.

Verdon, J. P., and J. J. Bommer (2021). Green, yellow, red, or out of the blue? An assessment of traffic light schemes to mitigate the impact of hydraulic fracturing-induced seismicity, *J. Seismol.* **25,** no. 1, 301–326, doi: 10.1007/s10950-020-09966-9.

Vernon, F., J. Tytell, M. A. H. Hedlin, K. Walker, R. Busby, and R. Woodward (2012). Integration of infrasound, atmospheric pressure, and seismic observations with the NSF EarthScope USArray transportable array, *EGU General Assembly Conference Abstracts*, 10,770 pp.

Wald, D. J. (2021). Comment on "Which earthquake accounts matter?" by Susan E. Hough and Stacey S. Martin, *Seismol. Res. Lett.* **93,** no. 1, 500–505, doi: 10.1785/0220210072.

Waxler, R., and J. Assink (2019). *Propagation Modeling Through Realistic Atmosphere and Benchmarking*, Springer International Publishing, Chambridge, 509–549, doi: 10.1007/978-3-319-75140-5_15.

Waxler, R., C. H. Hetzer, J. D. Assink, and P. Blom (2022). A two-dimensional effective sound speed parabolic equation model for infrasound propagation with ground topography, *J. Acoust. Soc. Am.* **152,** no. 6, 3659–3669.

Westaway, R., and P. L. Younger (2014). Quantification of potential macroseismic effects of the induced seismicity that might result from hydraulic fracturing for shale gas exploitation in the UK, *Q. J. Eng. Geol. Hydrogeol.* **47,** no. 4, 333–350, doi: 10.1144/qjegh2014-011.

Zhan, Z. (2019). Distributed acoustic sensing turns fiber-optic cables into sensitive seismic antennas, *Seismol. Res. Lett.* **91,** no. 1, 1–15, doi: 10.1785/0220190112.

Manuscript received 14 November 2022
Published online 7 July 2023